NEUROSCIENCE

Leukotriene A4 hydrolase inhibition improves age-related cognitive decline via modulation of synaptic function

Julia M. Adams, Sanket V. Rege, Angela T. Liu†, Ninh V. Vu, Sharda Raina, Douglas Y. Kirsher, Amy L. Nguyen, Reema Harish‡, Balazs Szoke, Dino P. Leone, Eva Czirr§, Steven Braithwaite, Meghan Kerrisk Campbell*

Leukotrienes, a class of inflammatory bioactive lipids, are well studied in the periphery, but less is known of their importance in the brain. We identified that the enzyme leukotriene A4 hydrolase (LTA4H) is expressed in healthy mouse neurons, and inhibition of LTA4H in aged mice improves hippocampal dependent memory. Single-cell nuclear RNA sequencing of hippocampal neurons after inhibition reveals major changes to genes important for synaptic organization, structure, and activity. We propose that LTA4H inhibition may act to improve cognition by directly inhibiting the enzymatic activity in neurons, leading to improved synaptic function. In addition, LTA4H plasma levels are increased in both aging and Alzheimer's disease and correlated with cognitive impairment. These results identify a role for LTA4H in the brain, and we propose that LTA4H inhibition may be a promising therapeutic strategy to treat cognitive decline in aging related diseases.

INTRODUCTION

Leukotrienes (LTs) are critical mediators of inflammation but have been studied only minimally in the central nervous system (CNS). However, our recent understanding of the role inflammation plays in the aging brain provides new questions of how LTs may be implicated. Aging is associated with a progressive decline in numerous functions and an increased incidence of diseases (*1*, *2*). The continuous, low-level inflammation in the absence of active infection that contributes to age-associated disease has been coined inflammaging (*3*). Inflammaging in the brain is characterized by increased neuroinflammation of astrocytes (*4*, *5*) and microglia (*6*, *7*), aberrant infiltration of immune cells into the parenchyma (*8*), loss of synapses (*9*, *10*), and impaired cognition (*6*, *11*, *12*). Inflammaging in the periphery (*13*, *14*) and within the brain (*15*–*17*) is detectable before the onset of disease symptoms, and failure to resolve this chronic inflammation has been hypothesized to be a major contributor to aging-related cognitive decline.

LTs are a group of biologically active lipid mediators (LTA4, LTB4, LTC4, LTD4, and LTE4), which are secreted from multiple cell types and play a critical role in recruiting leukocytes and other immune cells to sites of inflammation in the periphery (*18*). Cysteinyl LTs (Cys-LTs), LTC4, LTD4, and LTE4 have been shown to influence CNS diseases including traumatic brain injury, Alzheimer's disease (AD), Parkinson's disease (PD), multiple sclerosis, epilepsy, Huntington's disease, depression, and gulf war illness (*19*–*25*). However, the non–Cys-LTs, LTA4, and LTB4, which bind to Leukotriene B4 Receptor 1 (BLT1) and BLT2 receptors, respectively, LTB4R1 and LTB4R2 in mouse (*26*), are understudied in the brain. In the periphery, these G protein–coupled receptors are broadly expressed in leukocytes and are responsible for the chemotaxis of immune cells to sites of inflammation (*27*, *28*). Recently, LTB4 has been identified in the cerebral spinal fluid (CSF) of patients with AD, and LTB4 levels have been shown to increase with worsening cognitive diagnosis (*29*), suggesting that LTB4 may play a role in the brain similar to the Cys-LTs. The receptor for LTB4 (*30*) and upstream processing enzymes (*31*) are expressed in mouse and human neurons, and LTB4 has been detected in the brains of mice (*25*), but the role of LTB4 signaling in these brain cell types is unknown. In addition, in humans, the enzyme 5-lipoxygenase (5-LOX), which is upstream of LTA4 hydrolase (LTA4H), is increased in the brains of patients with AD (*32*), and ablation of 5-lipoxygenase–activating protein in an AD mouse model ameliorates cognitive impairment (*33*), prompting further investigation into the connection of LTA4H and cognition.

To better understand the role of LTB4 in the brain, we characterized the expression pattern of the LTB4 receptor LTB4R1 and processing enzyme LTA4H. We hypothesized that the reduction of LTB4 levels could have a direct impact on the function of neuronal cells that express LTB4R1 and LTA4H and tested two small-molecule LTA4H inhibitors: SC57461A (*34*, *35*) and AKST1220 in aged mice. We evaluated cognitive effects with behavioral experiments and performed RNA sequencing to investigate transcriptomic changes within neurons of the hippocampus. LTA4H inhibitors have been extensively studied in the clinic for peripheral inflammatory diseases (*36*), yet they are relatively understudied in CNS diseases. To address this, we measured LTA4H levels in human plasma, across age from healthy donors and patients with AD, and identified an increase in LTAH across aging and disease. Together, our findings identify a role for LTA4H in the brain and suggest that LTA4H inhibition may provide a therapeutic approach to treat cognitive decline.

Alkahest Inc., 125 Shoreway Road, Suite D, San Carlos, CA 94070, USA.
*Corresponding author. Email: meghan.campbell@grifols.com
†Present address: Altos Labs, 1300 Island Drive, Redwood City, CA 94065, USA.
‡Present address: Terns Pharmaceuticals, 1065 H Hillsdale Blvd., #100, Foster City, CA 94404, USA.
§Present address: Confluence Therapeutics, 329 Oyster Point Blvd, 3rd Floor, South San Francisco, CA 94080, USA.

RESULTS

LTA4H and LTB4R1 are localized to neurons

LTB4, a lipid signaling molecule, has been widely characterized throughout the periphery as a chemoattractant that recruits immune cells to sites of inflammation (*37*). More recently, it has been identified in the CSF of AD human patients (*29*), suggesting that this bioactive lipid may have functional consequences in the brain. To better understand whether LTB4 signaling could play a role in the CNS, brain expression of LTA4H, the enzyme responsible for its generation, was examined (Fig. 1A). LTA4H protein was detectable in crude brain cortex homogenates by Western blot (Fig. 1B). Via immunohistochemistry (IHC), LTA4H was found to be expressed in neurons, colocalizing with the nuclear maker NeuN throughout the brain (Fig. 1C). In addition, in the hippocampus, the *Lta4h* gene is highly expressed by approximately 10% of neurons (fig. S1 and table S1). The nuclear localization of LTA4H in other cell types, such as macrophages and basophils, was previously identified to be important for the coordination of LTB4 processing from arachidonic acid (AA) by first 5-LOX and subsequently LTA4H (Fig. 1A) (*38*). The unexpected identification of LTA4H in mouse neurons suggests that LTB4 may be synthesized in and secreted from neurons directly.

To understand where LTB4 signaling is occurring in the CNS, mouse brain tissue was stained for the high-affinity LTB4 receptor, LTB4R1, and its expression was detected along the dendrites of neurons and colocalized with microtubule-associated protein (MAP2) in the cortex and the cornu Ammonis 1 (CA1) region of the hippocampus (Fig. 1D). Furthermore, using biochemical fractionation of postsynaptic density (PSD)–enriched synaptic membranes, LTB4R1 was enriched in the membrane and extrasynaptic membrane fractions and is detectable in PSD-enriched fractions (Fig. 1E). Together, this characterization suggests that the inflammatory lipid LTB4 is both produced by and can signal to neurons within the mouse brain.

LTA4H inhibition modulates LT signaling in the brain

To determine the potential role of LTA4H in neurons, two specific and potent small-molecule inhibitors of LTA4H enzymatic function AKST1220 and SC57461A (figs. S2 to S4) were tested in aged mice. As plasma LTB4 levels were elevated in aged mice (Fig. 2A), plasma LTB4 levels were used to confirm compound efficacy in reduction of LTB4 levels in a target engagement assay (Fig. 2B and fig. S2), where both compounds show comparable levels of inhibition. LTA4H inhibition did not affect the LTB4 precursor lipid AA (fig. S3).

The expected binding modes of both small molecules to LTA4H are illustrated via molecular docking (Fig. 2, C to F) (*39*), demonstrating that AKST1220 and SC57461A bind in the hydrolase pocket of LTA4H and exhibit very similar amino acid interactions (Fig. 2F). The carboxylate substituents undergo polar contacts with the catalytic zinc responsible for hydrolysis of LTA4 to generate LTB4 (Fig. 1A), indicating that the mechanism of inhibition for both molecules is through competitive binding to the active site of the protein. Binding affinity calculations and ligand-enzyme energy scores also demonstrate that AKST1220 and SC57461A exhibit similar binding affinities toward human LTA4H (table S2).

Inhibition of LTA4H with AKST1220 in aged mice improves hippocampus-dependent cognitive impairment

To determine the impact of long-term LTA4H inhibition in aged mice, 20- to 22-month-old mice were dosed with AKST1220 or SC57461A. Mice dosed for 1 month using the SC57461A LTA4H inhibitor showed no statistically significant improvement in the y-maze spatial learning task (Fig. 3A) or in the radial arm water maze (RAWM) (fig. S5, A to D). Conversely, mice treated with AKST1220 for 1 month demonstrated improved cognitive performance in the y-maze (Fig. 3A and fig. S5D). To understand whether AKST1220 treatment could affect cognitive performance with a shorter dosing window, we tested the performance of aged mice using the contextual fear conditioning task following 10 days of dosing (Fig. 3B and fig. S5E) and identified enhanced cognitive performance with LTA4H inhibition. Furthermore, the detrimental effect of elevated LTA4H levels on cognition was further confirmed by direct administration of human recombinant protein to young mice (fig. S6).

Following a single oral dose of AKST1220 (10 mg/kg), aged mice have high concentrations found in total brain homogenate that persists up to 24 hours (Fig. 4A). Furthermore, AKST1220 was brain-penetrant at doses as low as 0.1 mg/kg (Fig. 4A). Conversely, SC57461A was not found to be brain-permeant (Fig. 4B) and, compared to AKST1220 at the same dose, was relatively undetectable (Fig. 4C). To better understand whether AKST1220 was entering the brain parenchyma or was bound within the brain vasculature, mice were dosed with ^{14}C-radiolabeled AKST1220 and imaged using micro-radioautography followed by IHC for the blood vessel maker lectin. Imaging revealed that ^{14}C-AKST1220 was broadly distributed throughout the brain. Silver grain particles of ^{14}C-AKST1220 were found both within blood vessels and in the brain parenchyma of the hippocampus (Fig. 4, D and E, and fig. S7). These results suggest that AKST1220 may have a direct impact not only on the peripheral LTA4H activity but also locally in the brain parenchyma, while SC57461A may function only by inhibiting LTA4H in the periphery.

LTA4H inhibition targets pathways responsible for synaptic organization, structure, and activity

To investigate the mechanism of improved cognition following chronic LTA4H inhibition, single nuclear RNA sequencing (Nuc-seq) was performed on hippocampal neurons (*40*) in aged mice following 1 month of LTA4H inhibitor treatment. Hippocampal nuclei were obtained from microdissected hippocampi that were processed following the 10x Genomics protocol for Nuc-seq, labeled with a phycoerythrin (PE)–conjugated anti-NeuN antibody, and enriched for neuronal nuclei using fluorescence-activated cell sorting (FACS; Fig. 5A and fig. S8). A total of 98,570 nuclei were isolated and profiled from three animals per treatment (30,744 nuclei from three AKST1220 treated animals, 31,402 nuclei from three SC57461A-treated animals, and 36,424 nuclei from three vehicle-treated animals). Low-quality nuclei (less than 1000 genes per nucleus) were removed, leaving a total of 93,683 nuclei with a mean of 3235 genes per nucleus that were retained for further processing (fig. S9). Unbiased clustering was performed on the nuclei using the Seurat R package [v4; (*41*, *42*)] and manually curated cell types using known marker genes, identifying CA1 and CA3 pyramidal neurons, dentate gyrus (DG) cells and a heterogeneous group of interneurons (IN) as shown by the uniform manifold approximation and projection (UMAP) plot (Fig. 5B). A small number of

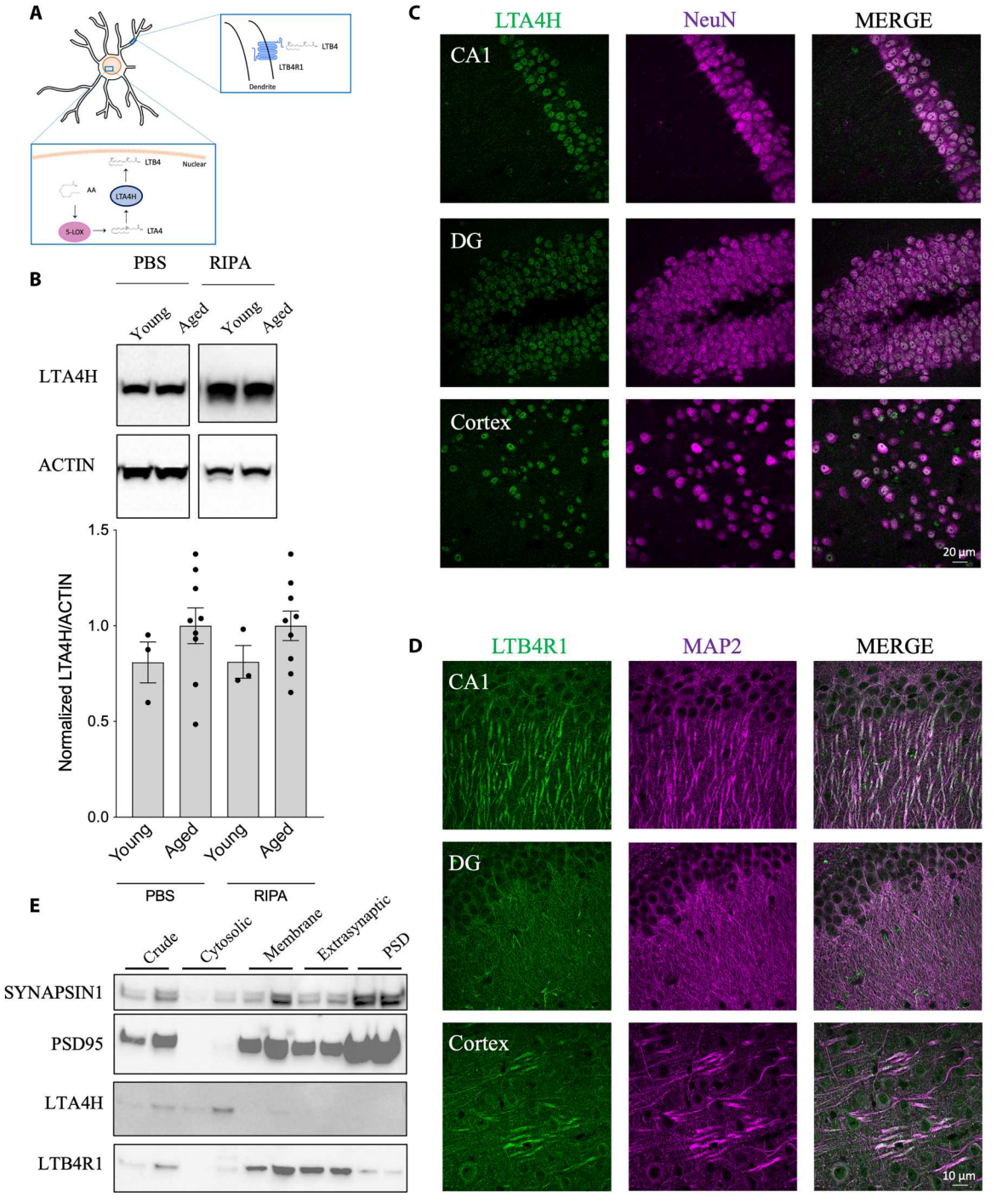

Fig. 1. LTA4H and LTB4R1 are localized to neurons. (**A**) Schematic depicting LTB4 processing and signaling in neurons. (**B**) LTA4H is detected in crude phosphate-buffered saline (PBS) and radioimmunoprecipitation assay (RIPA) Western blot homogenates from mouse cortex and is unchanged with age. Kruskal-Wallis test, $P = 0.3536$. All data shown as means ± SEM. (**C**) LTA4H is localized in the nucleus of neurons. Representative images of LTA4H (green) and NeuN (purple) in adult mouse brain. Scale bar, 20 µm. (**D**) LTB4R1 is localized along the dendrites of neurons. Representative images of LTBR41 (green) and MAP2 (purple) in adult mouse brain. Scale bar, 10 µm. (**E**) Biochemical postsynaptic density (PSD) enrichment from mouse hippocampus identified LTB4R1 to be enriched in membrane and extrasynaptic fractions. LTA4H is located within crude and cytosolic fractions. Presynaptic marker SYNAPSIN1 and postsynaptic maker PSD95 are used to show enrichment.

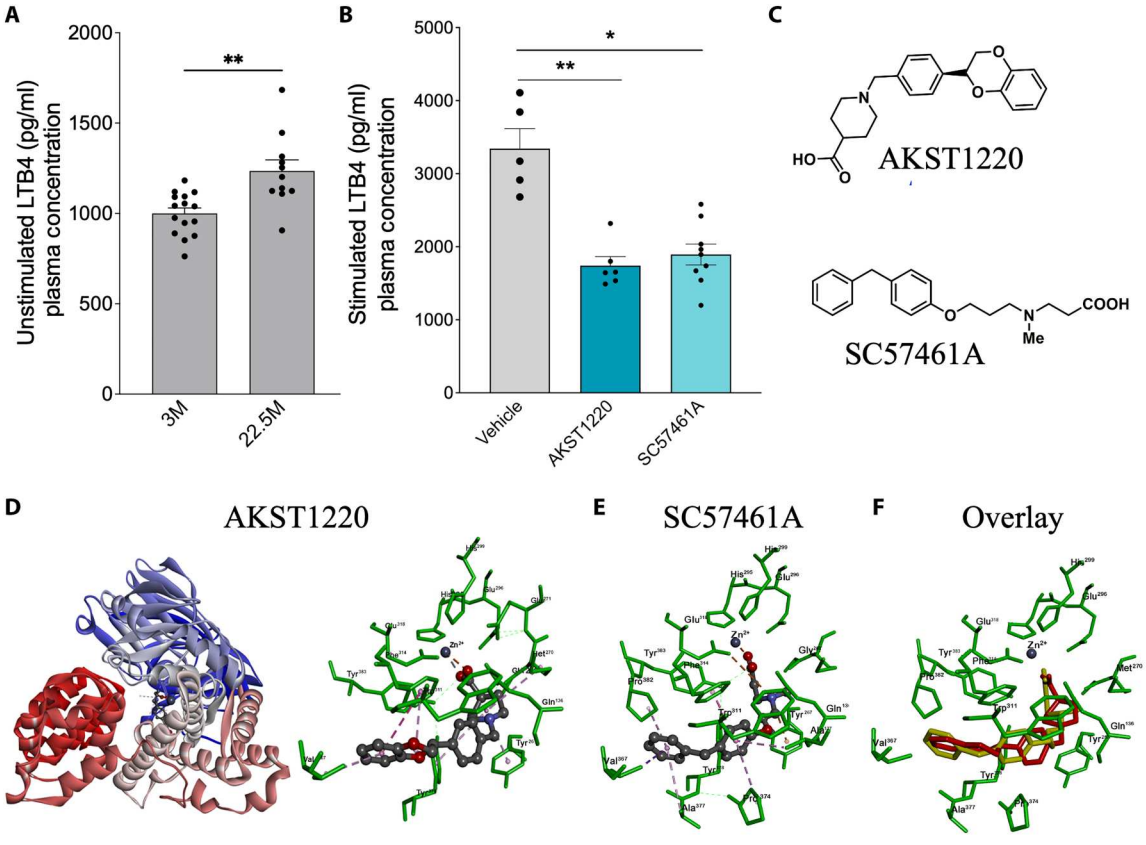

Fig. 2. AKST1220 and SC57461A are specific and potent small-molecule inhibitors of LTA4H. (**A**) Plasma LTB4 measured from unstimulated blood is significantly increased from 3 to 22.5 months (M). Unpaired *t* test, $^{**}P = 0.0011$, $F = 2.952$ ($n = 15$ and 11). (**B**) Plasma LTB4 levels from calcimycin-stimulated blood are significantly reduced following 4 weeks of dosing with LTA4H inhibitors AKST1220 or SC57461A. Kruskal-Wallis test, $P = 0.0006$ followed by Dunn's multiple comparisons: vehicle versus AKST1220, $^{**}P = 0.0034$; vehicle versus SC57461A, $^{*}P = 0.0212$; and AKST1220 versus SC57461A, $P > 0.9999$ ($n = 5$, 6, and 9). (**C**) Small-molecule structures of AKST1220 and SC57461A. (**D**) Molecular docking of AKST1220 into the structure of human LTA4H (Protein Data Bank ID: 6ENC). Right panel shows zoom in of hydrolase binding pocket (ball and stick cartoon) with individual interacting amino acids highlighted. (**E**) Molecular docking of SC57461A into the hydrolase binding pocket of human LTA4H. (**F**) Overlay of AKST1220 (red) and SC57461A (yellow) in the hydrolase binding pocket of human LTA4H shows similar binding modes of the two small molecules. All data are shown as means ± SEM.

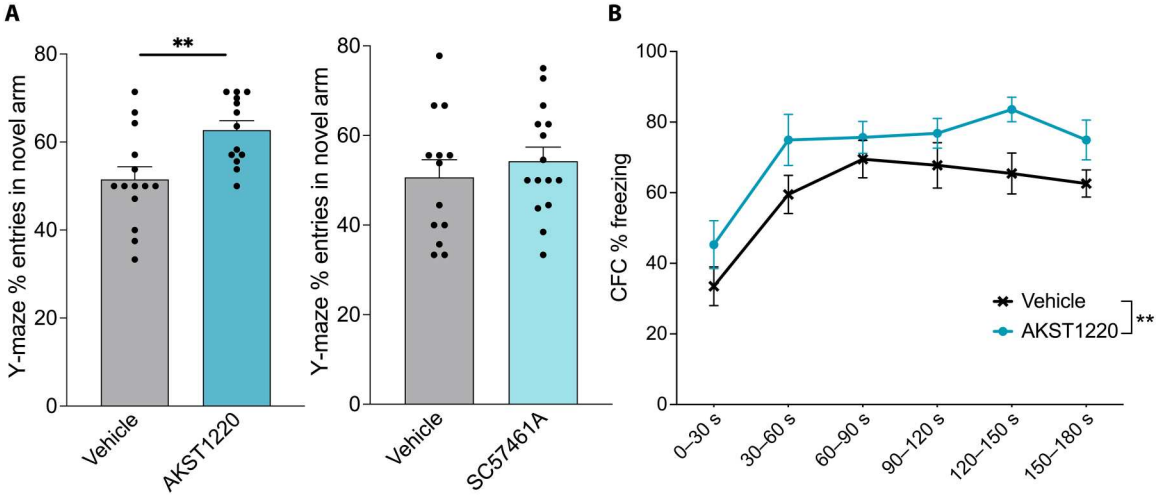

Fig. 3. LTA4H inhibition with AKST1220 improves cognition in aged mice. (**A**) Percent entries into the novel arm of the y-maze are significantly increased after 4 weeks of AKST1220 dosing compared to vehicle. Unpaired *t* test, $^{**}P = 0.0050$ ($n = 14$ and 13). Percent entries into the novel arm of the y-maze are unchanged after 4 weeks of SC57461A dosing compared to vehicle. Unpaired *t* test, $P = 0.4743$ ($n = 13$ and 15). (**B**) Contextual fear conditioning (CFC) is significantly improved after 10 days of AKST1220 treatment. Two-way analysis of variance (ANOVA) with repeated measures, $^{**}P = 0.007$, $F = 8.638$ ($n = 14$ and 14). All data are shown as means ± SEM.

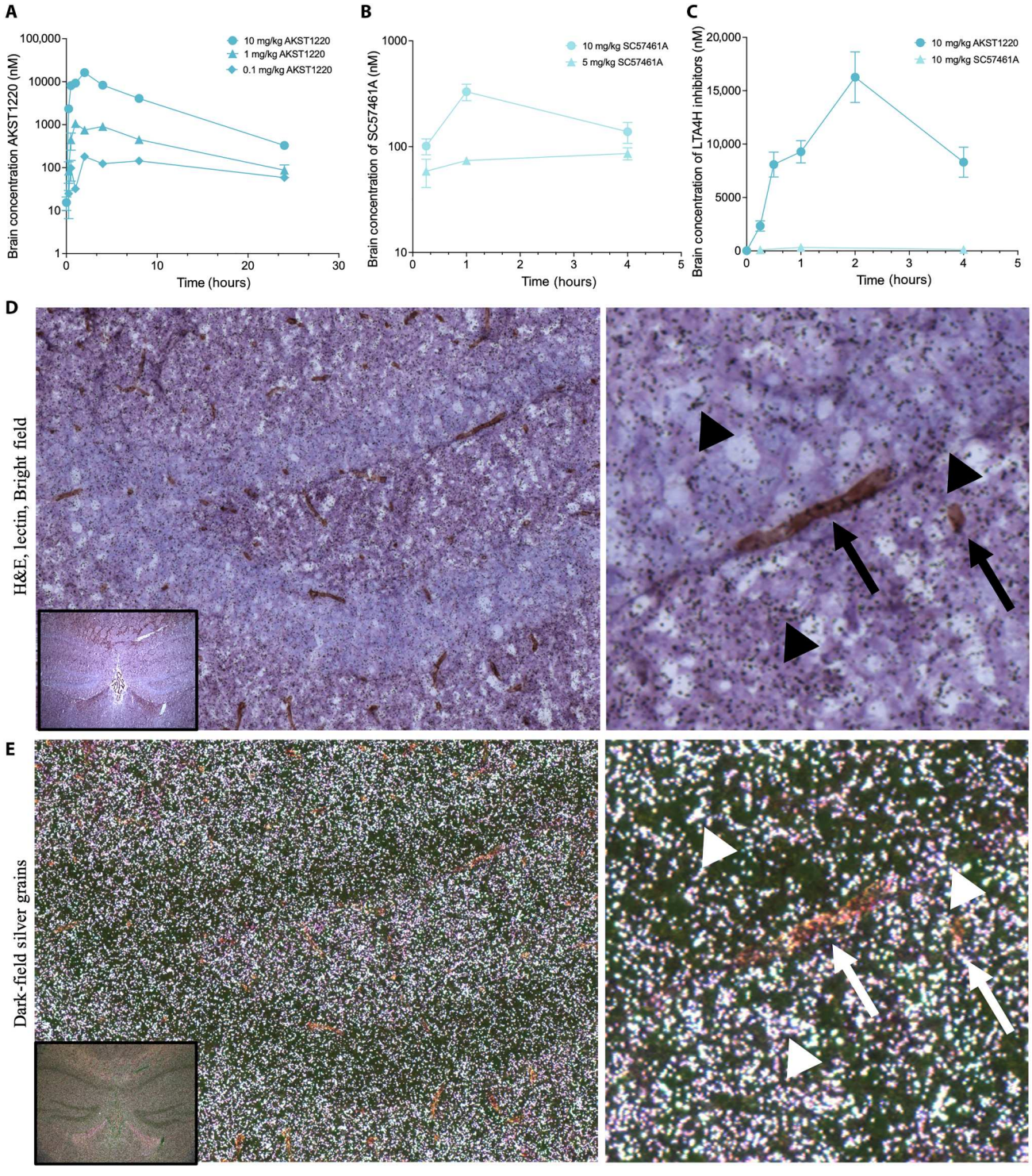

Fig. 4. AKST1220 is a brain-penetrant molecule. (**A**) Brain homogenate concentration of AKST1220 (nanomolar) following a single oral dose of 10, 1, or 0.1 mg/kg. (**B**) Brain homogenate concentration of SC57461A (nanomolar) following a single oral dose of 10 or 5 mg/kg. (**C**) Comparison of the brain homogenate concentrations of AKST1220 (A) and SC57461A (B) at 10 mg/kg. All data contain $n = 3$ mice per treatment group per time point at 20 months of age. All data are shown as means ± SEM. (**D**) Representative image of mouse midbrain after a single oral dose of ^{14}C-AKST1220 (small black particles) and subsequent immunohistochemical staining of biotinylated lectin (brown). Inset zoom in of the dentate gyrus (DG) with black arrows identifying blood vessels and arrowheads identifying AKST1220 in the brain parenchyma. H&E, with hematoxylin and eosin. (**E**) Dark-field image of (D) to visualize ^{14}C-AKST1220 silver grains as bright white particles on a dark background.

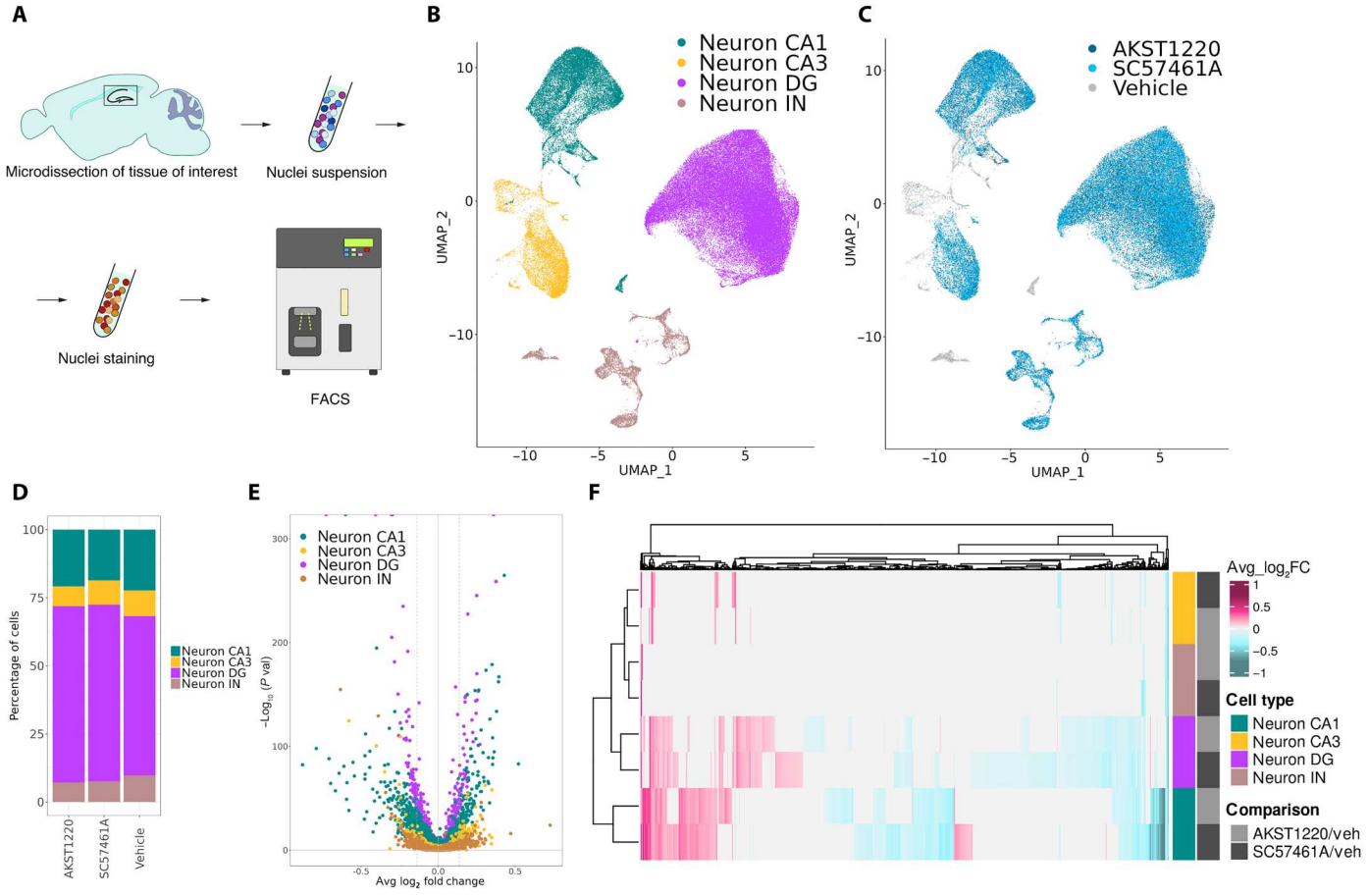

Fig. 5. LTA4H inhibition leads to cell-type–specific changes in gene expression in hippocampal neurons. (**A**) Schematic workflow for Nuc-seq: After microdissection, nuclei are stained against NeuN and sorted by fluorescence-activated cell sorting (FACS) for 10x Genomics single-nuclei processing. (**B**) Uniform manifold approximation and projection (UMAP) plot reveals robust separation of clusters identifying major neuronal cell types in the hippocampus. (**C**) UMAP plot colored by treatment paradigm reveals intermingling of cells within clusters. (**D**) Bar plot representing the relative contribution of cells from each treatment paradigm. (**E**) Volcano plot shows the results of differential gene expression changes between AKST1220 treatment and vehicle control in each cell type. Genes were considered differentially expressed if their FC of >1.1 or <−1.1 (dashed lines). (**F**) Hierarchically clustered top 2000 differentially expressed genes (DEGs) between LTA4H inhibitors AKST1220 against vehicle (mid-gray) and SC57461A against vehicle (dark gray) for the four major neuronal cell types. Red, increased expression after inhibitor treatment; blue, decreased expression after inhibitor treatment.

unidentified neuronal and nonneuronal cell types were excluded after the initial cell classification, retaining a total of 92,161 neuronal nuclei. LTA4H inhibition does not lead to obvious segregation of cells within the major cell-type clusters (Fig. 5C). Furthermore, the contribution from each treatment type to each of the major cell types is comparable, suggesting that LTA4H inhibition does not overtly affect cell-type distribution (Fig. 5D). Differentially expressed genes (DEGs) between LTA4H inhibition and vehicle treatment were computed for each major cell type using Seurat with the model-based analysis of single cell transcriptomics (MAST) differential test framework (*43*). DEGs with a fold change (FC) of ≥1.1 and an adjusted *P* value of <0.05 were considered statistically significant resulting in 425 DEGs for CA1 pyramidal neurons after AKST1220 treatment and 511 significant DEGs after SC57461A treatment compared to vehicle (Fig. 5E and table S3). To obtain an unbiased overview about DEGs between cell types and treatment comparisons, the top 2000 DEGs were selected from all major cell types across both comparisons, and hierarchical clustering was performed. The resulting heatmap reveals DEG fingerprints shared between treatments, most notably for CA1 pyramidal and DG cells (Fig. 5F and tables S4 and S5). Notably, IN and CA3 pyramidal neurons had fewer shared DEGs than CA1 and DG cells.

To better understand the differences between LTA4H inhibition by AKST1220 and SC57461A in cognition and brain penetrance, DEGs significantly modulated by AKST1220 treatment but unchanged with SC57461A were examined (tables S6 to S9). This analysis revealed a handful of interesting genes that could contribute to the differences in cognition observed between the two compounds. For example, *Ralyl* expression was increased in CA1 and DG following treatment with AKST1220 and was unchanged following SC57461A treatment. Higher expression of this gene has been linked to greater AD reserve, a phenomenon where individuals have a high burden of disease pathology but limited cognitive decline (*44*). In addition, decreased *Ralyl* expression is associated with AD (*45*) and PD (*45*, *46*), and genetic mutations have been identified in amyotrophic lateral sclerosis (ALS) (*47*). Conversely,

Lingo1 was down-regulated by AKST1220 but unchanged with SC57416A treatment. Knockdown or inhibition of *Lingo1* in neurodegenerative models protects animals from cognitive impairment in radial arm and y-mazes (*48*, *49*), possibly via enhancing neuronal survival (*50*, *51*) or decreasing amyloid-β production (*52*). Together, increased *Ralyl* or decreased *Lingo1* expression following AKST1220 treatment could contribute to the enhancement of cognition in aged mice and provide protection in patients with AD.

To determine the extent of similarities between DEGs from the two LTA4H inhibitors, the DEGs from both inhibitors were plotted as scatter plots: CA1 pyramidal neurons (Fig. 6A), DG neurons (Fig. 6B), and CA3 and IN (fig. S10). Consistent with the observations from the overview heatmap, the specific comparisons between the two inhibitors reveal strong correlations between AKST1220-treatment and SC57461A treatment for CA1 and DG (Pearson correlation coefficients of 0.92 and 0.90, respectively). Pathway enrichment analysis using gProfiler (Fig. 6C and fig. S11) (*53*) revealed a majority of terms with the highest enrichment *P* values in the source ontology "biological compartment" with synapse-related terms ranking among the highest. Similar to high correlations between the DEGs detected following the two inhibitor treatments, high correlations of the gene ontology (GO) enrichments were identified for CA1 pyramidal neurons (Fig. 6D) and DG neurons (Fig. 6E). Furthermore, the GO terms on the scatter plots show a strong correlation (Pearson correlation coefficients of 0.96 and 0.80, respectively) (Fig. 6, D and E). Together, these data highlight some of the similarities and differences between potential mechanisms underlying LTA4H inhibition between the two small molecules.

Inhibition of LTA4H in aged mice with AKST1220 resulted in improvements to hippocampus-dependent memory tasks, and GO pathway enrichment suggested a potential molecular mechanism for this improvement in synaptic organization, structure, and activity. To better understand these changes, some of the top DEGs up-regulated by LTA4H inhibition were first investigated (fig. S12 and tables S4 and S5). The CA1 and DG regions of the hippocampus were focused on because of their link to spatial and contextual learning and memory (*54*–*59*), and they had the strongest impact following LTA4H inhibition (Fig. 5F). For example, in CA1, the important excitatory synaptic genes *Cadm2* (avg_log$_2$FC AKST1220 = 0.15 and avg_log$_2$FC SC57461A = 0.13) and *Grin2a* (avg_log$_2$FC AKST1220 = 0.12 and avg_log$_2$FC SC57461A = 0.12) were significantly up-regulated. *Cadm2* encodes for synaptic cell adhesion molecule 2, which is responsible for forming homo- and heterodimeric complexes at synapses and is an important promoter of excitatory synaptic number (*60*). Similarly, *Grin2a* encodes for the 2A subunit of the ionotropic glutamate/*N*-methyl-D-aspartate receptor and is essential for the regulation of synaptic plasticity, synaptic strength, and memory (*61*, *62*).

In the periphery LTA4H plays a proinflammatory role (*18*, *63*). To understand whether LTA4H inhibition could affect cell types important for inflammation in the brain, microglia activation was quantified using the histological markers ionized calcium binding adaptor molecule 1 (Iba1) and CD68. Inhibition of LTA4H did not affect microglia activation measured by percent area of Iba1 or CD68 (fig. S13). Together with the transcriptomic results, these findings suggest that LTA4H inhibition in aged mice may improve age-related cognitive impairment by modulating gene expression responsible for changes in synaptic structure and function and not by affecting microglia cells responsible for proinflammatory signaling. As LTB4R1 is increased in PSD-enriched fractions of aged animals (Fig. 1E), these data link LTA4H inhibition with synaptic structure and function to improve cognitive impairment in aged mice.

LTA4H is increased with age and correlated with cognitive impairment in humans

To understand how LTA4H is further relevant to human biology, levels of LTA4H were measured from pools of plasma from young (18 years old) and aged (65+ years old) healthy human donors using two independent methods, enzyme-linked immunosorbent assay (ELISA) and an aptamer-based approach from SomaLogic, and found that LTA4H levels were significantly elevated in aged plasma (Fig. 7A and fig. S14). To determine the granularity of LTA4H plasma changes across different age ranges, healthy human plasma samples were quantified from donors in age brackets between 18 and 65+ years of age. The largest increase in LTA4H occurred between 18 and 30 years of age with only a more gradual increase in years after (Fig. 7B and fig. S14B).

To determine whether LTA4H levels are relevant to age-related human disease, the plasma from patient donors with different diagnoses of cognitive impairment: subjective cognitive decline (SCD), mild cognitive impairment (MCI), and AD diagnosis probable or possible (AD), was evaluated. A stepwise increase in LTA4H plasma levels was observed as the diagnosis of cognitive impairment worsened (Fig. 7C). Cognition is assessed in humans using the mini-mental state exam (MMSE), where a lower score indicates a higher level of cognitive impairment and a score of 24 or higher is considered to have no impairment. When plotting LTA4H plasma levels against MMSE test score at the time of collection, a strong negative correlation was found (Spearman $R = -0.1832712$, $P = 0.0034$) (Fig. 7D and fig. S15). Age was not identified as a confounding factor in this analysis, and there was no correlation with LTA4H plasma levels and age in this population of patients (fig. S15B), suggesting that, while LTA4H levels increase with healthy aging (Fig. 7), they can be further exacerbated with disease that is not age-dependent. Last, LTA4H plasma levels were also correlated with plasma levels of tau (Spearman $R = 0.1978$, $P = 0.0032$) (Fig. 7E), a plasma biomarker in AD (*64*), but LTA4H is not correlated with amyloid precursor protein plasma levels and was not changed across APOE genetic status (fig. S15, C and D). Together, this suggests that LTA4H has relevance in human biology and could be used as a potential plasma biomarker for AD or, more broadly, for cognitive impairment in patients.

DISCUSSION

In this study, we identify that LTA4H has a fundamental effect on the CNS in aging and disease related cognitive decline. We show that LTA4H and the LTB4 receptor LTB4R1 are expressed in neurons and that LTA4H inhibition improves cognition in aged mice. Using Nuc-seq and pharmacokinetic profiling, we propose that the mechanism of cognitive improvement may be by modulating important pathways for synaptic structure, organization, and function directly within neurons. As AKST1220 is brain permeable, we hypothesize that it may function by directly inhibiting neuronally expressed LTA4H within the CNS. However, AKST1220 and SC57461A also inhibit peripheral LTA4H and LTB4 production. Furthermore, SC57461A is not brain-penetrant while still affecting

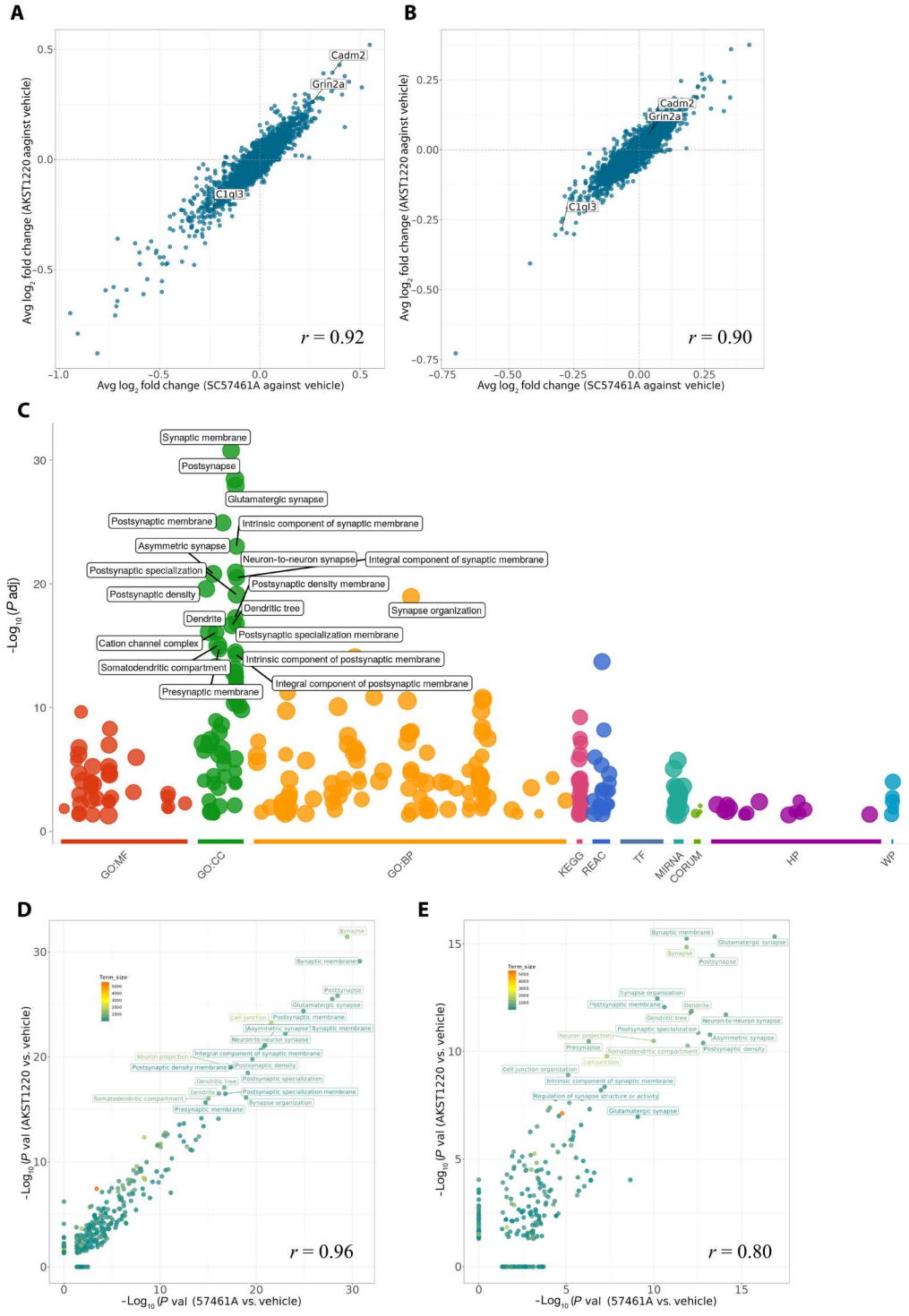

Fig. 6. LTA4H inhibitors lead to similar changes in gene expression and enriched pathways associated with synaptic organization, structure, and activity. (**A** and **B**) Scatter plots of $\log_2$ fold changes between LTA4H inhibitors AKST1220 (*y* axes) and SC57461A (*x* axes) for CA1 (A) and DG. (B) High correlation of DEGs between LTA4H inhibitors. (**C**) Gene ontology (GO) enrichment for top 500 genes in AKST1220 versus vehicle comparison for CA1 neurons reveals enrichment of synapse-associated terms. *Y* axis, $-\log_{10}$ (adjusted *P* value) of enrichment, *x* axis, and color-coded, ontology sources. MF, molecular function; CC, cellular compartment; BP, biological process; KEGG, Kyoto Encyclopedia of Genes and Genomes; REAC, reactome; TF, transcription factor; MIRNA, microRNA; CORUM, comprehensive resource of mammalian protein complexes; HP, human phenotype; WP, Wiki pathways. (**D** and **E**) Scatter plots of GO terms associated with both LTA4H inhibitors in CA1 (D) and DG (E). *X* axis, −log10 (adjusted *P* value) of enrichment terms for SC57461A treatment–associated terms; *y* axis, −log10 (adjusted *P* value) of enrichment terms for AKST1220 treatment–associated terms. Fill colors encode term sizes of enriched GO terms.

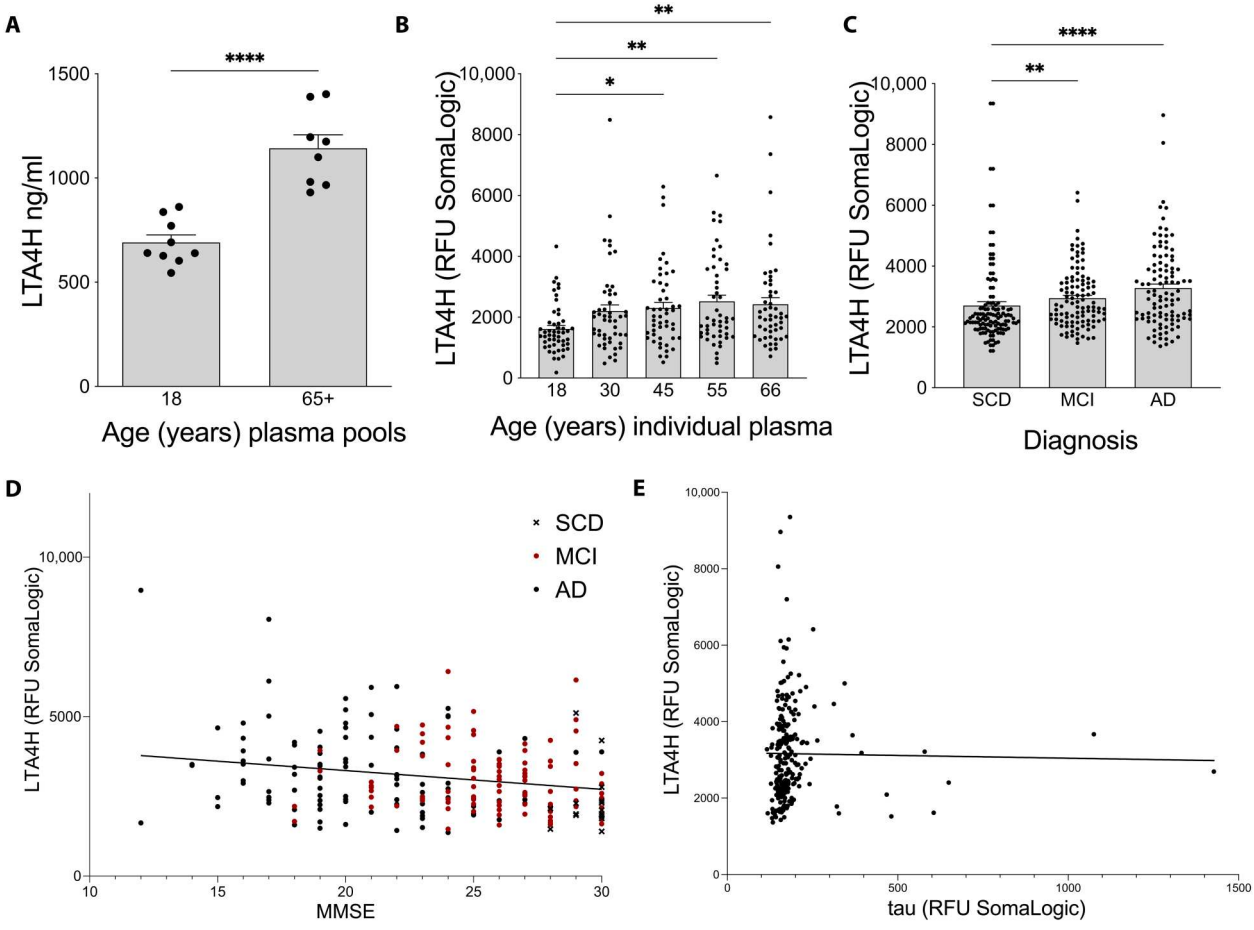

Fig. 7. LTA4H is increased in age and correlated with cognitive impairment in humans. (**A**) LTA4H levels (nanograms per milliliter) in pools of healthy human plasma measured by enzyme-linked immunosorbent assay (ELISA) are increased between 18 and 65 years of age. Five human plasma samples were pooled per age. Mann-Whitney test, ****$P < 0.0001$. $n = 9$ and 8. (**B**) LTA4H levels in individual healthy human plasma samples were measured by SomaLogic, and relative fluorescence units (RFU) show an increase with age. Kruskal-Wallis test, $P = 0.0023$ with Dunn's multiple comparisons: 18 versus 45, $P = 0.0198$; 18 versus 55, $P = 0.004$; and18 versus 66, $P = 0.0099$; $n = 50$ per age. (**C**) LTA4H levels in individual human plasma from patients diagnosed with subjective cognitive decline (SCD), mild cognitive impairment (MCI), or possible/probable AD measured by SomaLogic and RFU show an increase with higher cognitive impairment diagnosis. Kruskal-Wallis test, $P = 0.0023$ with Dunn's multiple comparisons: SCD versus MCI, $P = 0.0037$; and SCD versus AD, $P < 0.0001$; $n = 122$ (SCD), 106 (MCI), and 104 (AD). (**D**) Plasma levels of LTA4H measured in RFU at SomaLogic are correlated with mini-mental state exam (MMSE) score following correction for confounding factor of age. Age was found to not be a confounding factor in the comparison of LTA4H levels between AD, MCI, and SCD (fig. S9). Spearman $R = -0.1832712$, **$P = 0.0034$; $n = 254$. (**E**) Plasma levels of LTA4H are correlated with plasma levels of total tau measured in RFU at SomaLogic. Spearman $R = 0.1978$, **$P = 0.0032$; $n = 221$. All data are shown as means ± SEM.

neuronal gene expression pathways. Therefore, it is possible that reduction in peripheral LTB4 may also provide indirect improvements to neuronal health by reducing peripheral inflammation and increasing beneficial signaling cascades at the blood brain barrier (*65*). The LT signaling upstream and downstream of LTA4H have previously been shown to be important for brain capillary health (*66*–*68*). Therefore, future studies should explore the impacts of peripheral versus central LTA4H inhibition on brain endothelial cells and other neurovascular unit cell types. In addition, brain levels of LTB4 were unable to be measured from these studies using ELISA, likely due to a high matrix effect from brain lysate. Future studies should assess brain levels of LTB4 following LTA4H inhibition using more sensitive assays, such as purification of LTs by high-performance liquid chromatography (HPLC) followed by mass spectrometry (*69*).

We used molecular modeling of AKST1220 and SC57461A with the human LTA4H enzyme crystal structure and pharmacokinetic profiling to highlight the similarity of these two small-molecule inhibitors. We believe that these results provide an important path toward the aim of developing therapeutics to treat cognitive decline in aging and disease and provide a broad understanding of the potential molecular mechanisms of LTA4H inhibition in the brain. In addition to its hydrolase activity, LTA4H also has peptidase activity (*63*, *70*). The active sites for the peptidase and hydrolase activities are in close proximity within the structure of the enzyme (*39*), and both small molecules used in this study are predicted to inhibit the peptidase activity of LTA4H. However, the consequences of this additional activity were not explored in this study.

Single-cell nuclear RNA sequencing of hippocampal neurons in aged mice following LTA4H inhibition revealed changes to

important genes for synaptic organization, structure, and activity. For example, the Nuc-seq results identify changes to genes like *Cadm2* and *Grin2a* that suggest an overall improvement of synapse health, structure, and function. In addition, a handful of genes were identified to be significantly modulated by AKST1220 treatment but unchanged with SC57461A. Differences in gene expression of *Ralyl* and *Lingo1*, along with distinct brain penetrance profiles, could also contribute to the enhancement of cognition in aged mice observed with AKST1220, but not SC57461A. However, it is possible that the different doses of AKST1220 and SC57461A used in this study could explain the different effects observed in behavior. The dosing for each compound was chosen on the basis of the published literature (*34*, *35*, *71*). While the levels of LTA4H inhibition, measured by plasma LTB4, were comparable between each compound, the pharmacokinetic profile identified that SC57461A had slightly lower plasma levels than AKST1220 at the same dose. This finding suggests that SC57461A may be metabolized or cleared faster than AKST1220. Together, the differences in brain penetrance, differential gene expression, and pharmacokinetics likely contribute to the different behavioral outcomes between the two compounds.

For these findings to be applied to a potential therapeutic approach, LTA4H inhibition should be tested within a CNS model of neurodegeneration and neuroinflammation. These results would determine whether LTA4H inhibition can overcome the cognitive decline caused by aggressive disease pathologies, in addition to the improvement in age-related cognitive decline that we have identified here. Last, we highlight the potential of LTA4H as a plasma biomarker in AD and cognitive decline in humans. LTA4H plasma levels are increased in both aging and AD and correlated with cognitive impairment measured using MMSE, as well as plasma tau, which has been explored as a neurodegenerative protein driver (*64*, *72*). Further testing in clinical settings is necessary to apply LTA4H as a possible future biomarker for human disease. Overall, our study identifies a role for LTA4H in the brain and highlights the potential for the development of therapeutics and biomarkers for age-related cognitive decline and disease.

MATERIALS AND METHODS

Experimental design

The objective of this study was to characterize and understand the observation that LTA4H and LTB4R1 are expressed in mouse hippocampal neurons. We hypothesized that LTA4H and LTB4 could play a role in age-related cognitive decline and that inhibition of LTA4H may be a beneficial therapeutic strategy.

Animals

All animal handling and use was in accordance with Institutional Animal Care and Use Committee approved protocols (ALK-005). Male C57BL/6J mice were obtained from the Jackson Laboratory (Sacramento, CA) and shipped to Alkahest Inc. before the start of each study. Aged mice arrived at 17.5 months of aged and were further aged in house to between 20 and 22.5 months of age. Young mice arrived at 2 months and were further acclimated in house for at least 2 weeks before the start of dosing. Upon arrival, all mice were single-housed at standard temperature (22° ± 1°C) and in a light-controlled environment (lights on from 7:00 a.m. to 7:00 p.m.) with ad libitum access to food and water. Aged animals were subjected to a pretreatment open-field test before the initiation of dosing. Mouse weight, total distance traveled, and average velocity were used to evenly group animals between different treatment groups. Young mice were evenly distributed on the basis of weight alone. Different cohorts used in these findings are described in Table 1. All cohorts were on the background strain C57BL/6J, with the exception of cohort 9 used for the micro-autoradiography (mARG) study, which was performed using CD-1 mice.

Materials

Recombinant human LTA4H was purchased from R&D Systems (Minneapolis, MN) and underwent buffer exchange using a 3000-Da cutoff spin column (Thermo Fisher Scientific, Hampton, NH) to remove buffer components incompatible with in vivo dosing. The final concentration of LTA4H was determined by bicinchoninic acid (BCA) assay (Thermo Fisher Scientific, Waltham, MA). Vehicle and LTA4H were aliquoted in single use 1.5-ml O-ring tubes and stored at −80°C until needed for injections.

AKST1220 was synthesized at Boehringer Ingelheim (Ingelheim, Germany), previously having been explored in a rabbit atherosclerosis model (*71*) and was stored protected from light before experimentation. For behavioral studies, AKST1220 was formulated in 0.5% methylcellulose with 0.015% Tween 80 in water or 10% dimethyl sulfoxide (DMSO). For RNA sequencing and pharmacokinetic studies, AKST1220 was formulated in 45% hydroxypropyl-ß-cyclodextrin (pH 7; Sigma-Aldrich, St. Louis, MO). AKST1220 was made fresh every 5 to 7 days and stored at 4°C in between dosing sessions. SC57461A was purchased from Cayman Chemicals (Ann Arbor, MI) and was stored at −20°C in powdered form. A stock solution of 10 mg/ml was made in 100% DMSO and stored at −20°C until day of dosing. Stock solutions were thawed and diluted into sterile water immediately before each daily po (per os) dosing (1:9). If an entire vial of working solution was not used, then the vial was returned to −20°C until the next dosing day, where it was combined with new freshly thawed stock and made working solution vial for that day.

Dosing paradigms

For young mouse behavioral studies, 2-month-old mice were divided into two treatment groups of 14 to 15 mice each. Mice received a pulse dosing paradigm of 7 days of daily intravenous injections of 4.6 μg of recombinant human LTA4H or vehicle followed by behavioral testing and sacrifice 6 weeks later. For aged mouse behavioral studies, 19.5 to 20.8 months of age underwent 10 days or 4.7 weeks of daily po dosing with vehicle, AKST1220 (10 mg/kg), or SC57461A (5 mg/kg). Mice were euthanized 1 day following the conclusion of the last behavior test and 2 hours after the last dose.

For transcriptomic profiling, aged mice were divided into groups of 3 and administered either AKST1220 (1 mg/kg), SC57461A (2.5 mg/kg), or vehicle po two times a day for 4 weeks before sequencing. Mice were euthanized 2 hours after the last dose.

For pharmacokinetic analysis of AKST1220, aged mice were dosed by po with a single dose of AKST1220 at 10, 1, or 0.1 mg/kg. Mice were euthanized at times 0, 0.25, 0.5, 1, 2, 4, 8, and 24 hours after dose. Blood, brain, and plasma were collected, and pharmacokinetic analysis was performed at Quintara Discovery Inc. (Hayward, CA).

For pharmacokinetic analysis of SC57461A, aged mice were dosed by po with a single dose of SC57461A at 10 or 5 mg/kg.

Table 1. Description of mouse cohorts. NA, not applicable; po, per os (oral dosing); iv, intravenous; bid, two times a day; PK, pharmacokinetic; mARG, micro-autoradiography; IHC, immunohistochemistry.

Cohort	Treatment groups	Age (months)	Dose and treatment window	Figures
Cohort 1: young versus aged	Untreated	3	NA	Figs. 1B and 2A
		22.5		
Cohort 2: AKST1220	Vehicle and AKST1220	22.5	10 mg/kg, 4 weeks once daily po	Figs. 2B and 3 (A and B) and figs. S2 (E and F), S3A, S5D, and S13 (A and B)
Cohort 3: AKST1220	Vehicle and AKST1220	22.5	10 mg/kg, 10 days once daily po	Figs. 2B and 3A and figs. S2D and S5E
Cohort 4: SC57461A	Vehicle and SC57461A	22.5	5 mg/kg, 4 weeks once daily po	Fig. 3A and figs. S2G, S3B, S5 (A to D), and S13 (C and D)
Cohort 5: recombinant LTA4H	Vehicle and recombinant human LTA4H	3.5	4.6 μg/day for 7 days iv	fig. S6
Cohort 6: transcriptomics	Vehicle, AKST1220, and SC57461A	22.5	AKST1220, 1 mg/kg; SC57461A, 2.5 mg/kg bid, 4 weeks po	Figs. 5 and 6 and figs. S1 and S8 to S12
Cohort 7: PK AKST1220	Vehicle and AKST1220	20	Single dose of 10, 1, and 0.1 mg/kg po	Fig. 4 (A to C) and figs. S4 (A, C, D, and F) and S6
Cohort 8: PK SC57461A	Vehicle and SC57461A	20	Single dose of 10 and 5 mg/kg po	fig. S4 (B, C, E, and F)
Cohort 9: mARG + IHC	Vehicle and ^{14}C-AKST1220	3	Single dose of 10 mg/kg po	Fig. 4 (D and E) and fig. S7
Cohort 10: calcimycin stimulation assay	Untreated	18	NA	fig. S2A
Cohort 11: pilot dose response AKST1220	Vehicle and AKST1220	18	Single dose of 0.03, 0.1, and 0.3 mg/kg po	fig. S2B
Cohort 12: pilot dose response SC57461A	Vehicle and SC57461A	3	Single dose of 1.25, 2.5, and 5 mg/kg po	fig. S2C

Mice were euthanized at times 0.25, 1, and 4 hours after dose. Blood, brain, and plasma were collected, and pharmacokinetic analysis was performed at Quintara Discovery Inc. (Hayward, CA).

Behavioral paradigms

Open field

The open-field test was used before dosing in aged mice to randomize mice across treatment groups. Mice were brought into the experimental room for at least 30 min of acclimation to the experimental room conditions (dim lighting) before testing. Mice were placed individually into the center of a 16-in–by–16-in (0.40-m–by–0.40-m) box and allowed to explore for 15 min. The movements of the mice were recorded and tracked within a predefined peripheral and center (65% of total area) space using automated software (CleverSys, Reston, VA). In addition, the total distance and velocity were measured for duration of the test.

Y-maze

The y-maze was constructed of acrylic plastic; each arm is 15 in by 3 in, and the walls of the arms are 6 in high (0.38 m by 0.08 m by 0.15 m). Unique cues in the form of black shapes were adhered to walls at the ends of two of the arms (rising sun and swirl), while the third was un-cued and designated as the starting point for the mice. First, mice were individually placed in the starting arm and allowed to explore only one of the other two arms for 5 min; the second arm was blocked off with an acrylic plastic wall identical to that of the rest of the apparatus. After a 3-hour delay, the mouse was then returned to the maze with now both arms open to explore. All movements were recorded and tracked for analysis. The number of entries into and the time spent in each of the two arms, familiar and novel, was measured, as well as within the hub and start arm.

Contextual fear conditioning

Mice were brought into the testing room immediately before their trial to avoid exposure to sounds and scents from testing. Day 1: For training, mice were placed in the chambers, bright house light and fan on, for 2 min. Then, an auditory cue [2000 Hz, 70 dB; conditioned stimulus (CS)] was presented for 30 s. A 2-s foot shock (0.6 mA; unconditioned stimulus) was administered for the final 2 s of the CS. This procedure was repeated once, each after a 2-min interval, and the mouse was removed from the chamber 30 s after the second shock. The pans, chamber walls, and grid floors were cleaned with 70% ethanol between trials. Day 2: 24 hours after the training for aged mice and 3 days after the training for young mice, the mouse was returned to the same chamber in which the training occurred (memory for context), and freezing behavior was recorded for 3 min. The mouse was returned to its home cage. The pans, chamber walls, and grid floors were cleaned with 70% EtOH between trials.

Radial arm water maze

The water maze was filled with water at least 24 hours before the test to equilibrate to 23°C. The water was dyed with white latex paint to make the animals visible for tracking and to allow for the use of a hidden platform. Eight distinct visual cues were placed at the end of each arm of the RAWM inserts. On day-1 animals were given five trials each with a visible platform and a 30- to 60-min intertrial interval. Animals had 60 s to reach the platform. If they did not reach the platform in that time, they were guided to it and allowed to remain for 15 s before there were removed from the tank. The

goal arm remained constant, and a different start arm was randomly assigned for each of the five trials so that each mouse started in every arm once except for the two arms directly across from the platform. The goal arm was switched after every two to three mice and balanced between all treatment groups. After each trial, the mice were placed in an empty cage with blue pads and allowed to dry off under a heat lamp before being placed back into their home cage. Day 2 was the testing day, 48 hours after training, where animals were subjected to the same test of five trials each and a 30- to 60-min intertrial interval, but with a hidden platform. Animals were scored for number of errors (entry into a non-goal arm) and for latency to reach the platform. All trials were recorded using ANY-maze (Wood Dale, IL).

Histology

Mice were perfused with 0.9% saline transcardially. The brains were subsequently dissected and cut sagittally in two even halves. One-half was snap-frozen for later use in dry ice, and the other was fixed in 4% paraformaldehyde in phosphate-buffered saline (PBS) for use in IHC. After 2 days of fixation, the hemibrains were transferred to a 30% sucrose in PBS solution. Hemibrains were sectioned sagittally at 30 μm on a microtome at −22°C. Blocking was done on free floating sections in the appropriate serum at 10% serum in PBS with 0.5% Triton X-100. Primary antibodies were incubated overnight at 4°C at appropriate dilutions. Fluorescent secondary antibodies were applied the next day at a concentration of 1:300 for 1 hour at room temperature. Once mounted on slides, ProLong Gold Mounting Media (Thermo Fisher Scientific, Waltham, MA) was used to coverslip. The following primary antibodies were used in the IHC experiments: rabbit anti-LTA4H at 1:100 (Abcam, Cambridge, UK), rabbit anti-BLT1 (LTB4R1) at 1:200 (Cayman Chemical, Ann Arbor, MI), mouse anti-NeuN (Millipore, Burlington, MA) at 1:500, guinea pig anti-MAP2 at 1:200 (Synaptic Systems, Göttingen, Germany), mouse anti-CD68 (Bio-Rad, Hercules, California) at 1:1000, and rat anti-Iba1 (Wako Chemicals, Richmond, VA) at 1:2500. Images were acquired using the Axio Scan.Z1 (Zeiss, Oberkochen, Germany) at 20× or a Zeiss LSM800 with Airyscan at 63× and Airyscan processed using Zen Blue 2.5 (Zeiss, Oberkochen, Germany).

Plasma sample collection and processing

Mouse plasma samples and calcimycin stimulation

For calcimycin-stimulated samples, whole mouse blood was collected by cardiac puncture using heparin as an anti-coagulant and incubated for 15 min in 37C/5% CO_2. During this time, a 0.1 mM calcimycin stock was made by diluting 10 mM calcimycin (Sigma-Aldrich, A23187) formulated in DMSO into PBS. Control solution was made by diluting the same volume of DMSO in PBS. Both solutions were sonicated for 10 min in a 37°C water bath. Calcimycin (0.1 mM; stimulated) or control solution (unstimulated) was added to each well of whole blood and incubated at 37C/5% CO_2 for 30 min. Whole blood was spun for 10 min at 1000*g* to separate out plasma. Calcimycin stimulation is used to increase the dynamic range of the assay by releasing the intracellular pools of LTB4 (*73*, *74*).

Human plasma samples aging cohort

The first set of plasma samples was collected from healthy male donors of 18, 30, 45, 55, and 65 to 68 (average 66) years of age by plasmapheresis as part of standard plasma collection for Grifols Biomat USA source plasma. "Retain tubes" of individual donations containing 3 ml of citrate plasma were stored at −30°C. Only samples from "infrequent donations" (collected >60 days after preceding plasma donation) were used. Plasma samples of 40 individuals per age group were pooled into eight pools of five samples each for proteomic analysis. A second set of plasma samples was collected from healthy male and female plasma donors of 18- to 22-year-old subjects and 55- to 65-year-old subjects by venipuncture as part of plasma donation at Access Biologicals (Vista, CA). Samples containing either EDTA or citrate plasma were frozen at −30°C and subsequently were aliquoted and stored at −80°C until use. Aging plasma samples were acquired at Grifols or Access Biologicals for commercial purposes. All donors gave written consent before plasma donation.

Human AD plasma samples

Plasma samples, demographic, clinical, and cognitive information, including MMSE scores, were used for analysis from patients with SCD (n = 122), MCI (n = 106), and AD dementia (n = 104) from the Memory Clinic at Ace Alzheimer Center Barcelona (*75*). EDTA plasma samples were shipped frozen to Alkahest, aliquoted, and stored at −80°C until use. Aliquoting for proteomic analysis of all three sets of plasma samples was carried out as follows: Original frozen plasma samples were thawed on ice, centrifuged at 3200*g* for 30 min at 0°C, and filtered through 0.22-μm MillexGV filter (MilliporeSigma, Burlington, MA) to remove cryoprecipitate. Filtrate was aliquoted into cryotubes and stored at −80°C until use. Cognitive assessment using the MMSE was performed at the Memory Clinic at Ace Alzheimer Center, and data were provided to Alkahest as individual MMSE values. All participants gave written consent, and the protocol was approved by the Ethics Committee of the Hospital Clinic i Provincial (Barcelona, Spain) (EudraCT: 2014–000798-38) (*75*).

Enzyme-linked immunosorbent assays

LTB4 plasma quantifications

Mouse LTB4 levels were detected by running an ELISA on the collected stimulated and unstimulated plasma diluted 1:10 (Enzo Life Sciences, ADI-901-068; R&D Systems, KGE006B). The ELISA plates were read on a BMG LABTECH CLARIOstar plate reader at 405 nm.

LTA4H plasma quantifications

Human plasma was diluted 1:500 and analyzed for LTA4H using LSBio Human LTA4H Sandwich ELISA Kit (LS-F22077-1). The ELISA was read on a BMG LABTECH CLARIOstar plate reader at 450 nm.

AA plasma quantifications

Mouse AA plasma levels were detected by running an ELISA on the collected unstimulated plasma diluted 1:10 (Abcam, ab287798). The ELISA plates were read on a BMG LABTECH CLARIOstar plate reader at 450 nm.

Western blot

After perfusion, brains were taken out, and cortex was subdissected into hippocampus and cortical cap before being frozen on dry ice. Tissue was homogenized first in PBS using the Bead Ruptor, homogenates were centrifuged at max speed (~21,330*g*) for 10 min at 4°C, and then supernatants were collected for subsequent analysis of the soluble fraction. A second radioimmunoprecipitation assay (Thermo Fisher Scientific, Waltham, MA) homogenization of the

PBS pellet was performed with the same procedure described above. All steps were performed with the addition of a protease inhibitor cocktail (Thermo Fisher Scientific, Waltham, MA). The protein concentration was quantified using a Pierce BCA protein assay kit (Thermo Fisher Scientific, Waltham, MA). Samples were then normalized to 25 μg per well and reduced with lithium dodecyl sulfate (LDS) before being electrophoresed onto Bolt 4 to 12% Bis-Tris Plus Gel (Invitrogen, Waltham, MA). Gels were turbo-transferred to Trans-Blot Turbo Mini Nitrocellulose membranes (Bio-Rad, Hercules, CA). Blocking was done in a 5% milk solution (Bio-Rad, Hercules, CA) in Tris-buffered saline with 0.5% Tween (TBST) and incubated with 1:5000 rabbit anti-LTA4H (Abcam, Cambridge, UK) overnight at 4°C. Blots were imaged following incubation with horseradish peroxidase (HRP)–conjugated secondary antibodies at 1:5000 (Thermo Fisher Scientific, Hampton, NH) for 1 hour at room temperature and subsequently with SuperSignal West Pico PLUS Chemiluminescent Substrate (Thermo Fisher Scientific, Waltham, MA). Blots were imaged on a Bio-Rad Chemidoc and quantified using Image Lab 6.0 (Bio-Rad, Hercules, CA) software. Samples were randomized across gels and run blinded in single replicates. Blots were stripped and reprobed for ACTIN-HRP (Cell Signaling Technology, Danvers, MA) at 1:5000 overnight at 4°C as a loading control.

For PSD-enrichment preparation, protocol was adapted from Wiggins *et al.* (*76*). Hippocampus was subdissected before being homogenized in 0.32 M sucrose buffer containing 10 mM Hepes and 1 mM EDTA. Some of the sample was saved for "crude fraction." Samples were then centrifuged three times to remove unhomogenized, insoluble material and then spun again to separate cytosolic and pellet fractions. Supernatant from this step was collected and labeled as "cytosolic fraction." Pellet was washed twice with 4 mM Hepes/1 mM EDTA, resuspended, and then spun. Pellet was then resuspended in sucrose buffer with 0.5% Triton X-100 and incubated for 15 min to obtain "membrane fraction." Then, samples were centrifuged, and supernatant was collected as "extrasynaptic membrane fraction." Samples were resuspended in sucrose buffer with 1% Triton X-100, 1% SDS, and 1% sodium deoxycholate; incubated for 1 hour; and then centrifuged to yield "PSD-enriched fraction." Protein quantification and western blotting were performed as stated above with the following antibodies: SYNAPSIN1 (Cell Signaling Technology, Danvers, MA) at 1:1000, PSD95 (Cell Signaling Technology, Danvers, MA) at 1:1000, LTA4H (Abcam, Cambridge, UK) at 1:5000, and LTB4R1 (Cayman Chemical, Ann Arbor, MI) at 1:200.

RNA sequencing

After 4 weeks of dosing, aged mice were anesthetized 2 hours after the final dosing using isoflurane and transcardially perfused with 20 ml of ice-cold artificial cerebrospinal fluid (*77*). Hippocampi were microdissected from three mice per treatment group and processed for nuclei isolation for 10x Genomics single-nuclei sequencing following the manufacturer's guidelines (10x Genomics Sample Preparation Demonstrated Protocol CG000124; 10x Genomics, Pleasanton, CA) with the following modification: Lysis incubation time was increased to 4 min. Nuclei were stained for NeuN using a PE-conjugated anti-NeuN antibody (1:1000; EMD Millipore, FCMAB317PE) and counterstained with DRAQ5 (1:5000; Thermo Fisher Scientific, PI62251) for 30 min on ice to allow separation of nuclei from debris particles using a Sony MA900 FACS sorter (Sony Biotechnology, San Jose, CA). Eight samples of 8000 nuclei each were collected per treatment group and immediately processed for 10x single-nuclei sequencing using the 10x Genomics Chromium Next GEM Single Cell 3′ Reagent Kits v3.1 Dual Index (CG000315 Rev. B). Single-nuclei libraries were sequenced on an Illumina NovaSeq 6000 to a target depth of ~50,000 reads per cell. Raw sequencing reads were processed using 10x Genomics Cell Ranger (v6.0; with the option –include-introns) and aligned against Gencode GRCm39, release M26. Libraries were processed using Seurat [v4; (*41*, *42*, *78*)], and nuclei were classified using known marker genes. Briefly, the following marker genes were used for cell classification: CA1 (Npcd, Stxbp1, Tcf4, Wfs1, Dcn, Calb1, Nov, and Rorb), CA3 (Tmem150a, Plagl1, Fmo1, Prkcd, Socs2, Serpinf1, Kctd4, and Dkk3), DG (Iqgap2, Gpr161, Prox1, Tdo2, Slc39a6, Slc26a10, Crlf1, Sema5a, Abcb10, Gpc4, and Stxbp6), and IN (Gad1, Gad2, Pvalb, Sst, Vip, Calb2, Ndnf, Smad3, Reln, and Npy). Cells with ambiguous signatures or low signal (<500 genes per cell), and nonneuronal cell types were filtered out. Differential gene expression was computed using Seurat's FindMarker function with MAST (*43*), and GO enrichment was performed using gProfiler2 (*53*); briefly, for each comparison, DEGs were ranked [abs($\log_2$FC) × −$\log_{10}$ (*P* val)], and the top 500 ordered genes were submitted to gProfiler2. All genes with an average expression above threshold (0.01 in Seurat's "data" slot) per cell type were used as custom background list for GO queries. Volcano, scatter, and bar plots were generated using ggplot2 (*79*) (https://ggplot2.tidyverse.org), and heatmaps were generated using the R package ComplexHeatmap (*80*).

Pharmacokinetic analysis

Brain, blood, and plasma samples for bioanalysis of AKST1220 or SC57461A were collected and prepared at Alkahest. Brain samples were homogenized with two volumes of ice-cold water. Heparin blood was collected by cardiac puncture. An aliquot of blood was collected, and an aliquot was spun for 10 min at 1000*g* to separate out plasma. Aliquots of brain lysate, whole blood, and plasma were frozen and shipped on dry ice to Quintara Discovery Inc. (Hayward, CA) for bioanalysis.

At Quintara, an aliquot of 20 μl of each plasma sample or plasma-diluted tissue homogenate was extracted with 140 μl of acetonitrile containing internal standard (dexamethasone at 50 ng/ml). The mixtures were vortexed on a shaker for 15 min and subsequently centrifuged at 3200*g* for 15 min. A 110-μl aliquot was then transferred to a fresh plate for injection into the liquid chromatography–tandem mass spectrometry. Calibration standards and quality control samples were prepared by spiking the test compound into control mouse plasma or brain homogenate and then processed with the unknown samples.

Molecular docking methodology

The molecular docking studies were carried out using the computational software Discovery Studio (DS) Structure-Based-Design software from Dassault Systems Biovia Corp., San Diego, USA (v20.1.0.19295). The three-dimensional (3D) structure of AKST1220 and SC57461A was prepared using the Small Molecules module in DS using CHARMm force field at pH 7.4 and was energy-minimized using the Smart Minimizer with 2000 minimization steps (root mean square gradient = 0.01 kcal/mol) and distance-dependent dielectric constant at pH 7.4 (*81*, *82*). The solved

x-ray structure of human LTA4H was obtained from Research Collaboratory for Structural Bioinformatics (RCSB) data bank (Protein Data Bank ID: 6ENC) (*39*). The protein was prepared after removing water using the Prepare Proteins option under the Macromolecules module in DS using CHARMm force field. A binding sphere of 10 Å was prepared using the Receptor-Ligand Interactions module in DS after selecting the bound compound 11. The compound 11 was deleted, and molecular docking studies were carried out using the 3D structure of AKST1220 or SC57461A prepared earlier. The CDOCKER algorithm[2] in the Receptor-Ligand Interactions module was used for molecular docking studies. The CDOCKER algorithm is based on a simulated annealing protocol and included 2000 heating steps to reach the target temperature of 700 K followed by 5000 cooling steps and a target temperature of 300 K. The root mean square deviation was calculated using the Structure module in DS. The top 10 docked binding modes of AKST1220 and SC57461A in human LTA4 hydrolase obtained were evaluated on the basis of the CDOCKER energy and CDOCKER interaction energy scores (kilocalories per mole). The ligand-enzyme interactions for the top ranked binding mode were evaluated by investigating the type of polar and nonpolar interactions and their distance parameters (*81*, *82*). The binding affinities of AKST1220 and SC57461A in kilocalories per mole was calculated using the equation $E_{binding}$ = energy of complex ($E_{ligand\text{-}receptor}$) − energy of ligand ($E_{ligand}$) − energy of receptor ($E_{receptor}$) and the implicit solvent function generalized Born with a simple switching.

SomaScan assay (SomaLogic) methodology

Plasma samples were analyzed by the Soma Scan multiplex proteomic profiling platform measuring 1305 protein analytes at SomaLogic Inc. (Boulder, CO) as described (*83*). Briefly, test samples were incubated with a mixture of proprietary aptamer-based affinity reagents called SOMAmers. Two sequential bead-based immobilization and washing steps eliminated unbound or nonspecifically bound proteins and the unbound SOMAmers, leaving only protein target-bound SOMAmers. These remaining SOMAmers were isolated, and each reagent quantified simultaneously on a custom Agilent hybridization array.

Proximity extension assay (O-link) methodology

Relative concentrations of 981 unique proteins (all analytes of 12 O-link Proteomics panels: Cardiometabolic, Cell Regulation, CVD II, CVD III, Development, Immune Response, Immuno-Oncology, Inflammation, Metabolism, Neurology, Oncology, Organ Damage) were measured in the plasma samples by proximity extension assay (PEA) technology (Assarsson) at Olink Analysis Service (Watertown, MA). The PEA immunoassay relies on simultaneous dual target recognition by matched antibody pairs that are labeled by complementary oligonucleotide sequences. When both antibodies bind to the target protein, the oligonucleotide tags hybridize, and extension results in a DNA reporter that is quantified by real-time quantitative polymerase chain reaction. Protein levels are reported in NPX (Normalized Proteine eXpression), Olink's arbitrary unit that is in $\log_2$ scale (*84*). Assay characteristics and validation data, like detection limit, precision, and validated sample types, are available from the Olink website: www.olink.com/resources-support/document-download-center/#validationdata.

mARG and IHC

Brain penetrance of AKST1220 was measured using mARG followed by IHC at Pharmaron UK Limited. AKST1220 was radiolabled with ^{14}C with a specific activity of 58 mCi/mmol quantified by liquid scintillation counting. The radiochemical purity of the ^{14}C-AKST1220 was determined using radioHPLC and was ≥95% before use in the study. Male CD-1 mice were ordered from Charles River Laboratories and subjected to health examination before enrollment in the study. All animals were in the weight range of 27 to 29 g and approximately 8 to 12 weeks old at the time of dose administration.

Five minutes before administration of ^{14}C-AKST1220, a single intravenous dose of biotinylated lectin (Vector Laboratories) was administered at 1.5 mg/kg. Mice received a single oral dose of ^{14}C-AKST1220 at 10 mg/kg (radioactive dose of 1 mCi/kg) in 45% HP-β-cyclodextrin (w/v; MilliporeSigma, product number H5784-10ML) in H_2O and pH adjusted to pH 6 with 1 M NaOH. The required quantities of each radiolabeled test item were combined with the nonradiolabeled test item as appropriate to achieve a radioactive concentration. All dosing solutions were prepared fresh the same day as the dosing.

Two male CD-1 mice each received a single oral administration of ^{14}C-AKST1220, following predosing with biotinylated lectin at a dose level detailed in section. An additional animal also received a dose of dose vehicle to act as a control for background radioactivity following a biotinylated lectin predose administration. Mice were euthanized at 2 hours after dose, by overdose of carbon dioxide gas, followed by cervical dislocation. Immediately after sacrifice of each animal, the brain was removed and cut transversely into three separate portions to allow analysis of the forebrain, midbrain, and cerebellum. Each brain portion was rapidly frozen in isopentane and cooled to around −35°C with solid CO_2 in an appropriately sized plastic mold containing embedding medium. Blocked samples were stored in precooled, labeled bags at −80°C until required for sectioning. A frozen tissue block was removed from storage and attached to a precooled specimen disc using embedding medium. The resulting block was trimmed using a Leica CM3050S cryomicrotome, until a good cross section of tissue was observed. Under safe-light conditions, sections (5 μm in thickness) were transferred onto glass microscope slides that were precoated with nuclear emulsion. Sufficient sections were cut to allow processing of slides at different exposure intervals. Ten slides were prepared for each of four exposure time points (1, 2, 4, and 6 weeks). Slides were exposed in light-tight boxes at −20°C for the duration of the exposure period. Each box contained a desiccant to prevent accumulation of moisture. At each specified exposure time, slides were removed from storage and allowed to equilibrate to room temperature in the sealed box for approximately 1 hour. Under safe-light conditions, slides were developed and fixed, after which time they were able to be handled under normal-light conditions.

Following development for mARG, slides were rinsed in distilled water and fixed in 10% neutral buffered formalin for 3 min. Following washing, slides were incubated with a Vectastain Elite ABC kit for 45 min. Slides were washed again and incubated with 3,3′-diaminobenzidene and substrate for 10 min. Slides were washed, stained with hematoxylin and eosin, and then coverslipped for imaging. Digital images were generated to show the localization of the radioactivity at cellular resolution. Separate sections collected onto uncoated microscope slides were exposed against phosphor-imaging plates for 7 days. At completion of the exposure period,

imaging plates were scanned using an Amersham Typhoon IP Phosphor imager, and images were obtained to show the gross distribution of radioactivity within the brain sections. Slides processed for mARG were visually assessed using a Zeiss Axio Imager.A2 light microscope. Representative digital images were captured using a Retiga 2000R CCD camera (QImaging) with associated Image-Pro Premier v9.1 software (MediCybernetics).

Statistical analysis

Values represented in bar graphs are shown as means, and error bars represent SEM. Graphs were generated using GraphPad Prism. All statistical tests are represented in the figure legends along with n and P values. For $n > 10$ with normally distributed data, parametric tests were used; otherwise, nonparametric tests were used.

Supplementary Materials

This PDF file includes:
Figs. S1 to S15
Tables S1 to S9

Other Supplementary Material for this manuscript includes the following:
Excel files S1 to S9

REFERENCES AND NOTES

1. Y. Hou, X. Dan, M. Babbar, Y. Wei, S. G. Hasselbalch, D. L. Croteau, V. A. Bohr, Ageing as a risk factor for neurodegenerative disease. *Nat. Rev. Neurol.* **15**, 565–581 (2019).
2. C. Lopez-Otin, M. A. Blasco, L. Partridge, M. Serrano, G. Kroemer, The hallmarks of aging. *Cell* **153**, 1194–1217 (2013).
3. C. Franceschi, J. Campisi, Chronic inflammation (inflammaging) and its potential contribution to age-associated diseases. *J. Gerontol. A Biol. Sci. Med. Sci.* **69**, S4–S9 (2014).
4. M. M. Boisvert, G. A. Erikson, M. N. Shokhirev, N. J. Allen, The aging astrocyte transcriptome from multiple regions of the mouse brain. *Cell Rep.* **22**, 269–285 (2018).
5. B. T. Kress, J. J. Iliff, M. Xia, M. Wang, H. S. Wei, D. Zeppenfeld, L. Xie, H. Kang, Q. Xu, J. A. Liew, B. A. Plog, F. Ding, R. Deane, M. Nedergaard, Impairment of paravascular clearance pathways in the aging brain. *Ann. Neurol.* **76**, 845–861 (2014).
6. R. Britton, A. T. Liu, S. V. Rege, J. M. Adams, L. Akrapongpisak, D. Le, R. Alcantara-Lee, R. A. Estrada, R. Ray, S. Ahadi, I. Gallager, C. F. Yang, S. S. Minami, S. P. Braithwaite, E. Czirr, M. K. Campbell, Molecular and histological correlates of cognitive decline across age in male C57BL/6J mice. *Brain Behav.* **12**, e2736 (2022).
7. A. Niraula, J. F. Sheridan, J. P. Godbout, Microglia priming with aging and stress. *Neuropsychopharmacology* **42**, 318–333 (2017).
8. H. Scheiblich, M. Trombly, A. Ramirez, M. T. Heneka, Neuroimmune connections in aging and neurodegenerative diseases. *Trends Immunol.* **41**, 300–312 (2020).
9. J. H. Morrison, M. G. Baxter, The ageing cortical synapse: Hallmarks and implications for cognitive decline. *Nat. Rev. Neurosci.* **13**, 240–250 (2012).
10. T. Wyss-Coray, Ageing, neurodegeneration and brain rejuvenation. *Nature* **539**, 180–186 (2016).
11. M. Weber, T. Wu, J. E. Hanson, N. M. Alam, H. Solanoy, H. Ngu, B. E. Lauffer, H. H. Lin, S. L. Dominguez, J. Reeder, J. Tom, P. Steiner, O. Foreman, G. T. Prusky, K. Scearce-Levie, Cognitive deficits, changes in synaptic function, and brain pathology in a mouse model of normal aging(1,2,3). *eNeuro* **2**, ENEURO.0047–ENEU15.2015 (2015).
12. L. Aron, J. Zullo, B. A. Yankner, The adaptive aging brain. *Curr. Opin. Neurobiol.* **72**, 91–100 (2022).
13. W. Cao, H. Zheng, Peripheral immune system in aging and Alzheimer's disease. *Mol Neurodegener* **13**, 51 (2018).
14. C. E. Finger, I. Moreno-Gonzalez, A. Gutierrez, J. F. Moruno-Manchon, L. D. McCullough, Age-related immune alterations and cerebrovascular inflammation. *Mol. Psychiatry* **27**, 803–818 (2022).
15. G. Zhang, J. Li, S. Purkayastha, Y. Tang, H. Zhang, Y. Yin, B. Li, G. Liu, D. Cai, Hypothalamic programming of systemic ageing involving IKK-β, NF-κB and GnRH. *Nature* **497**, 211–216 (2013).
16. S. Gordleeva, O. Kanakov, M. Ivanchenko, A. Zaikin, C. Franceschi, Brain aging and garbage cleaning: Modelling the role of sleep, glymphatic system, and microglia senescence in the propagation of inflammaging. *Semin. Immunopathol.* **42**, 647–665 (2020).
17. M. Lopez-Teros, A. Alarcon-Aguilar, N. E. Lopez-Diazguerrero, A. Luna-Lopez, M. Konigsberg, Contribution of senescent and reactive astrocytes on central nervous system inflammaging. *Biogerontology* **23**, 21–33 (2022).
18. M. P. Y. Michael Shim, "Leukotriene A4 hydrolase—An evolving therapeutic target," in *Inflammatory Diseases - Immunopathology, Clinical and Pharmacological Bases*, M. Khatami, Ed. (InTech, 2012), chap. 12, pp. 253–278.
19. A. Ghosh, F. Chen, A. Thakur, H. Hong, Cysteinyl leukotrienes and their receptors: Emerging therapeutic targets in central nervous system disorders. *CNS Neurosci. Ther.* **22**, 943–951 (2016).
20. K. J. Herbst-Robinson, L. Liu, M. James, Y. Yao, S. X. Xie, K. R. Brunden, Inflammatory eicosanoids increase amyloid precursor protein expression via activation of multiple neuronal receptors. *Sci. Rep.* **5**, 18286 (2015).
21. J. Marschallinger, I. Schaffner, B. Klein, R. Gelfert, F. J. Rivera, S. Illes, L. Grassner, M. Janssen, P. Rotheneichner, C. Schmuckermair, R. Coras, M. Boccazzi, M. Chishty, F. B. Lagler, M. Renic, H. C. Bauer, N. Singewald, I. Blumcke, U. Bogdahn, S. Couillard-Despres, D. C. Lie, M. P. Abbracchio, L. Aigner, Structural and functional rejuvenation of the aged brain by an approved anti-asthmatic drug. *Nat. Commun.* **6**, 8466 (2015).
22. S. S. Tang, M. J. Ji, L. Chen, M. Hu, Y. Long, Y. Q. Li, M. X. Miao, J. C. Li, N. Li, H. Ji, X. J. Chen, H. Hong, Protective effect of pranlukast on $A\beta_{1-42}$-induced cognitive deficits associated with downregulation of cysteinyl leukotriene receptor 1. *Int. J. Neuropsychopharmacol.* **17**, 581–592 (2014).
23. S. S. Tang, X. Y. Wang, H. Hong, Y. Long, Y. Q. Li, G. Q. Xiang, L. Y. Jiang, H. T. Zhang, L. P. Liu, M. X. Miao, M. Hu, T. T. Zhang, W. Hu, H. Ji, F. Y. Ye, Leukotriene D4 induces cognitive impairment through enhancement of $CysLT_1$ R-mediated amyloid-β generation in mice. *Neuropharmacology* **65**, 182–192 (2013).
24. X. Y. Wang, S. S. Tang, M. Hu, Y. Long, Y. Q. Li, M. X. Liao, H. Ji, H. Hong, Leukotriene D4 induces amyloid-β generation via CysLT1R-mediated NF-κB pathways in primary neurons. *Neurochem. Int.* **62**, 340–347 (2013).
25. S. Attaluri, R. Upadhya, M. Kodali, L. N. Madhu, D. Upadhya, B. Shuai, A. K. Shetty, Brain-specific increase in leukotriene signaling accompanies chronic neuroinflammation and cognitive impairment in a model of Gulf war illness. *Front. Immunol.* **13**, 853000 (2022).
26. T. Yokomizo, Two distinct leukotriene B_4 receptors, BLT1 and BLT2. *J. Biochem.* **157**, 65–71 (2015).
27. A. M. Tager, A. D. Luster, BLT1 and BLT2: The leukotriene B_4 receptors. *Prostaglandins Leukot. Essent. Fatty Acids* **69**, 123–134 (2003).
28. T. Yokomizo, T. Izumi, K. Chang, Y. Takuwa, T. Shimizu, A G-protein-coupled receptor for leukotriene B_4 that mediates chemotaxis. *Nature* **387**, 620–624 (1997).
29. K. V. Do, E. Hjorth, Y. Wang, B. Jun, M. I. Kautzmann, M. Ohshima, M. Eriksdotter, M. Schultzberg, N. G. Bazan, Cerebrospinal fluid profile of lipid mediators in Alzheimer's disease. *Cell. Mol. Neurobiol.*, (2022).
30. C. Emre, E. Hjorth, K. Bharani, S. Carroll, A. C. Granholm, M. Schultzberg, Receptors for pro-resolving mediators are increased in Alzheimer's disease brain. *Brain Pathol.* **30**, 614–640 (2020).
31. J. Michael, M. S. Unger, R. Poupardin, P. Schernthaner, H. Mrowetz, J. Attems, L. Aigner, Microglia depletion diminishes key elements of the leukotriene pathway in the brain of Alzheimer's disease mice. *Acta Neuropathol. Commun.* **8**, 129 (2020).
32. M. D. Ikonomovic, E. E. Abrahamson, T. Uz, H. Manev, S. T. Dekosky, Increased 5-lipoxygenase immunoreactivity in the hippocampus of patients with Alzheimer's disease. *J. Histochem. Cytochem.* **56**, 1065–1073 (2008).
33. P. F. Giannopoulos, J. Chiu, D. Pratico, Learning impairments, memory deficits, and neuropathology in aged tau transgenic mice are dependent on leukotrienes biosynthesis: Role of the cdk5 kinase pathway. *Mol. Neurobiol.* **56**, 1211–1220 (2019).
34. L. J. Askonas, J. F. Kachur, D. Villani-Price, C. D. Liang, M. A. Russell, W. G. Smith, Pharmacological characterization of SC-57461A (3-[methyl[3-[4-(phenylmethyl)phenoxy]propyl] amino]propanoic acid HCl), a potent and selective inhibitor of leukotriene A_4 hydrolase I: In vitro studies. *J. Pharmacol. Exp. Ther.* **300**, 577–582 (2002).
35. J. F. Kachur, L. J. Askonas, D. Villani-Price, N. Ghoreishi-Haack, S. Won-Kim, C. D. Liang, M. A. Russell, W. G. Smith, Pharmacological characterization of SC-57461A (3-[methyl[3-[4-(phenylmethyl)phenoxy]propyl]amino]propanoic acid HCl), a potent and selective inhibitor of leukotriene A_4 hydrolase II: In vivo studies. *J. Pharmacol. Exp. Ther.* **300**, 583–587 (2002).
36. R. J. Snelgrove, Leukotriene A_4 hydrolase: An anti-inflammatory role for a proinflammatory enzyme. *Thorax* **66**, 550–551 (2011).
37. R. He, Y. Chen, Q. Cai, The role of the LTB4-BLT1 axis in health and disease. *Pharmacol. Res.* **158**, 104857 (2020).

38. T. G. Brock, E. Maydanski, R. W. McNish, M. Peters-Golden, Co-localization of leukotriene a4 hydrolase with 5-lipoxygenase in nuclei of alveolar macrophages and rat basophilic leukemia cells but not neutrophils. *J. Biol. Chem.* **276**, 35071–35077 (2001).
39. S. Numao, F. Hasler, C. Laguerre, H. Srinivas, N. Wack, P. Jager, A. Schmid, A. Osmont, P. Rothlisberger, J. Houguenade, C. Bergsdorf, J. Dawson, N. Carte, A. Hofmann, C. Markert, L. Hardaker, A. Billich, R. M. Wolf, C. A. Penno, B. Bollbuck, W. Miltz, T. A. Rohn, Feasibility and physiological relevance of designing highly potent aminopeptidase-sparing leukotriene A4 hydrolase inhibitors. *Sci. Rep.* **7**, 13591 (2017).
40. B. Lacar, S. B. Linker, B. N. Jaeger, S. R. Krishnaswami, J. J. Barron, M. J. E. Kelder, S. L. Parylak, A. C. M. Paquola, P. Venepally, M. Novotny, C. O'Connor, C. Fitzpatrick, J. A. Erwin, J. Y. Hsu, D. Husband, M. J. McConnell, R. Lasken, F. H. Gage, Nuclear RNA-seq of single neurons reveals molecular signatures of activation. *Nat. Commun.* **7**, 11022 (2016).
41. A. Butler, P. Hoffman, P. Smibert, E. Papalexi, R. Satija, Integrating single-cell transcriptomic data across different conditions, technologies, and species. *Nat. Biotechnol.* **36**, 411–420 (2018).
42. T. Stuart, A. Butler, P. Hoffman, C. Hafemeister, E. Papalexi, W. M. Mauck 3rd, Y. Hao, M. Stoeckius, P. Smibert, R. Satija, Comprehensive integration of single-cell data. *Cell* **177**, 1888–1902.e21 (2019).
43. G. Finak, A. McDavid, M. Yajima, J. Deng, V. Gersuk, A. K. Shalek, C. K. Slichter, H. W. Miller, M. J. McElrath, M. Prlic, P. S. Linsley, R. Gottardo, MAST: A flexible statistical framework for assessing transcriptional changes and characterizing heterogeneity in single-cell RNA sequencing data. *Genome Biol.* **16**, 278 (2015).
44. Y. Zhang, J. Wang, X. Liu, H. Liu, Exploring the role of RALYL in Alzheimer's disease reserve by network-based approaches. *Alzheimers Res. Ther.* **12**, 165 (2020).
45. J. P. Bennett, P. M. Keeney, RNA- sequencing reveals similarities and differences in gene expression in vulnerable brain tissues of Alzheimer's and Parkinson's diseases. *J. Alzheimers Dis. Rep.* **2**, 129–137 (2018).
46. H. Liu, Y. Huang, J. Li, Bioinformatic analysis for the identification of key candidate genes and pathways in the substantia nigra in Parkinson's disease. *J. Integr. Neurosci.* **17**, 619–631 (2018).
47. C. J. Chen, C. M. Chen, T. W. Pai, H. T. Chang, C. S. Hwang, A genome-wide association study on amyotrophic lateral sclerosis in the Taiwanese Han population. *Biomark. Med.* **10**, 597–611 (2016).
48. Q. He, L. Jiang, Y. Zhang, H. Yang, C. N. Zhou, Y. H. Xie, Y. M. Luo, S. S. Zhang, L. Zhu, Y. J. Guo, Y. H. Deng, X. Liang, Q. Xiao, L. Zhang, J. Tang, D. J. Huang, Y. N. Zhou, X. Y. Dou, F. L. Chao, Y. Tang, Anti-LINGO-1 antibody ameliorates cognitive impairment, promotes adult hippocampal neurogenesis, and increases the abundance of CB1R-rich CCK-GABAergic interneurons in AD mice. *Neurobiol. Dis.* **156**, 105406 (2021).
49. R. He, W. Han, X. Song, L. Cheng, H. Chen, L. Jiang, Knockdown of Lingo-1 by short hairpin RNA promotes cognitive function recovery in a status convulsion model. *3 Biotech* **11**, 339 (2021).
50. S. Mi, X. Lee, Z. Shao, G. Thill, B. Ji, J. Relton, M. Levesque, N. Allaire, S. Perrin, B. Sands, T. Crowell, R. L. Cate, J. M. McCoy, R. B. Pepinsky, LINGO-1 is a component of the Nogo-66 receptor/p75 signaling complex. *Nat. Neurosci.* **7**, 221–228 (2004).
51. H. Inoue, L. Lin, X. Lee, Z. Shao, S. Mendes, P. Snodgrass-Belt, H. Sweigard, T. Engber, B. Pepinsky, L. Yang, M. F. Beal, S. Mi, O. Isacson, Inhibition of the leucine-rich repeat protein LINGO-1 enhances survival, structure, and function of dopaminergic neurons in Parkinson's disease models. *Proc. Natl. Acad. Sci. U.S.A.* **104**, 14430–14435 (2007).
52. Y. Bai, K. Markham, F. Chen, R. Weerasekera, J. Watts, P. Horne, Y. Wakutani, R. Bagshaw, P. M. Mathews, P. E. Fraser, D. Westaway, P. St George-Hyslop, G. Schmitt-Ulms, The in vivo brain interactome of the amyloid precursor protein. *Mol. Cell. Proteomics* **7**, 15–34 (2008).
53. L. Kolberg, U. Raudvere, I. Kuzmin, J. Vilo, H. Peterson, gprofiler2 -- An R package for gene list functional enrichment analysis and namespace conversion toolset g:Profiler. *F1000Res* **9**, ELIXIR-709 (2020).
54. T. Bartsch, J. Dohring, A. Rohr, O. Jansen, G. Deuschl, CA1 neurons in the human hippocampus are critical for autobiographical memory, mental time travel, and autonoetic consciousness. *Proc. Natl. Acad. Sci. U.S.A.* **108**, 17562–17567 (2011).
55. J. Ji, S. Maren, Differential roles for hippocampal areas CA1 and CA3 in the contextual encoding and retrieval of extinguished fear. *Learn. Mem.* **15**, 244–251 (2008).
56. J. Z. Tsien, P. T. Huerta, S. Tonegawa, The essential role of hippocampal CA1 NMDA receptor-dependent synaptic plasticity in spatial memory. *Cell* **87**, 1327–1338 (1996).
57. V. C. Piatti, L. A. Ewell, J. K. Leutgeb, Neurogenesis in the dentate gyrus: Carrying the message or dictating the tone. *Front. Neurosci.* **7**, 50 (2013).
58. A. Treves, A. Tashiro, M. P. Witter, E. I. Moser, What is the mammalian dentate gyrus good for? *Neuroscience* **154**, 1155–1172 (2008).
59. S. Trouche, B. Bontempi, P. Roullet, C. Rampon, Recruitment of adult-generated neurons into functional hippocampal networks contributes to updating and strengthening of spatial memory. *Proc. Natl. Acad. Sci. U.S.A.* **106**, 5919–5924 (2009).
60. M. Missler, T. C. Sudhof, T. Biederer, Synaptic cell adhesion. *Cold Spring Harb. Perspect. Biol.* **4**, a005694 (2012).
61. J. E. Hanson, K. Ma, J. Elstrott, M. Weber, S. Saillet, A. S. Khan, J. Simms, B. Liu, T. A. Kim, G. Q. Yu, Y. Chen, T. M. Wang, Z. Jiang, B. M. Liederer, G. Deshmukh, H. Solanoy, C. Chan, B. D. Sellers, M. Volgraf, J. B. Schwarz, D. H. Hackos, R. M. Weimer, M. Sheng, T. M. Gill, K. Scearce-Levie, J. J. Palop, GluN2A NMDA receptor enhancement improves brain oscillations, synchrony, and cognitive functions in Dravet syndrome and Alzheimer's disease models. *Cell Rep* **30**, 381–396.e4 (2020).
62. F. Li, J. Z. Tsien, Memory and the NMDA receptors. *N. Engl. J. Med.* **361**, 302–303 (2009).
63. R. J. Snelgrove, P. L. Jackson, M. T. Hardison, B. D. Noerager, A. Kinloch, A. Gaggar, S. Shastry, S. M. Rowe, Y. M. Shim, T. Hussell, J. E. Blalock, A critical role for LTA_4H in limiting chronic pulmonary neutrophilic inflammation. *Science* **330**, 90–94 (2010).
64. N. Mattsson, H. Zetterberg, S. Janelidze, P. S. Insel, U. Andreasson, E. Stomrud, S. Palmqvist, D. Baker, C. A. Tan Hehir, A. Jeromin, D. Hanlon, L. Song, L. M. Shaw, J. Q. Trojanowski, M. W. Weiner, O. Hansson, K. Blennow, Plasma tau in Alzheimer disease. *Neurology* **87**, 1827–1835 (2016).
65. L. Schurer, S. Corvin, F. Rohrich, C. Abels, A. Baethmann, Leukocyte/endothelial interactions and blood-brain barrier permeability in rats during cerebral superfusion with LTB4. *Acta Neurochir. Suppl.* **60**, 51–54 (1994).
66. A. M. S. Hartz, R. G. Rempe, E. L. B. Soldner, A. Pekcec, J. Schlichtiger, R. Kryscio, B. Bauer, Cytosolic phospholipase A2 is a key regulator of blood-brain barrier function in epilepsy. *FASEB J.* **33**, 14281–14295 (2019).
67. K. L. Black, J. T. Hoff, Leukotrienes increase blood-brain barrier permeability following intraparenchymal injections in rats. *Ann. Neurol.* **18**, 349–351 (1985).
68. A. M. Hartz, A. Pekcec, E. L. Soldner, Y. Zhong, J. Schlichtiger, B. Bauer, P-gp protein expression and transport activity in rodent seizure models and human epilepsy. *Mol. Pharm.* **14**, 999–1011 (2017).
69. G. Dawson, Measuring brain lipids. *Biochim. Biophys. Acta* **1851**, 1026–1039 (2015).
70. L. Orning, J. K. Gierse, F. A. Fitzpatrick, The bifunctional enzyme leukotriene-A4 hydrolase is an arginine aminopeptidase of high efficiency and specificity. *J. Biol. Chem.* **269**, 11269–11273 (1994).
71. C. Calcagno, O. Lairez, J. Hawkins, S. W. Kerr, M. S. Dugas, T. Simpson, J. Epskamp, P. M. Robson, M. Eldib, I. Bander, P. K-Raman, S. Ramachandran, A. Pruzan, A. Kaufman, V. Mani, A. Ehlgen, H. G. Niessen, J. Broadwater, Z. A. Fayad, Combined PET/DCE-MRI in a rabbit model of atherosclerosis: Integrated quantification of plaque inflammation, permeability, and burden during treatment with a leukotriene A4 hydrolase inhibitor. *JACC Cardiovasc. Imaging* **11**, 291–301 (2018).
72. H. Zetterberg, K. Blennow, Moving fluid biomarkers for Alzheimer's disease from research tools to routine clinical diagnostics. *Mol Neurodegener.* **16**, 10 (2021).
73. P. Gresele, J. Arnout, M. C. Coene, H. Deckmyn, J. Vermylen, Leukotriene B_4 production by stimulated whole blood: Comparative studies with isolated polymorphonuclear cells. *Biochem. Biophys. Res. Commun.* **137**, 334–342 (1986).
74. R. J. Pueringer, C. C. Bahns, M. M. Monick, G. W. Hunninghake, A23187 stimulates translocation of 5-lipoxygenase from cytosol to membrane in human alveolar macrophages. *Am. J. Physiol.* **262**, L454–L458 (1992).
75. I. de Rojas, J. Romero, O. Rodriguez-Gomez, P. Pesini, A. Sanabria, A. Perez-Cordon, C. Abdelnour, I. Hernandez, M. Rosende-Roca, O. Sotolongo-Grau, A. Mauleon, L. Vargas, M. Alegret, A. Espinosa, G. Ortega, S. Gil, M. Guitart, A. Gailhajanet, M. A. Santos-Santos, S. Moreno-Grau, S. Ruiz, L. Montrreal, E. Martin, E. Peleja, F. Lomena, F. Campos, A. Vivas, M. Gomez-Chiari, M. A. Tejero, J. Gimenez, V. Perez-Grijalba, G. M. Marquie, G. Monte-Rubio, S. Valero, A. Orellana, L. Tarraga, M. Sarasa, A. Ruiz, M. Boada, F. study, Correlations between plasma and PET beta-amyloid levels in individuals with subjective cognitive decline: The Fundacio ACE Healthy Brain Initiative (FACEHBI). *Alzheimers Res. Ther.* **10**, 119 (2018).
76. A. T. Wiggins, A. M. Pacchioni, P. W. Kalivas, Integrin expression is altered after acute and chronic cocaine. *Neurosci. Lett.* **450**, 321–323 (2009).
77. J. T. Ting, T. L. Daigle, Q. Chen, G. Feng, Acute brain slice methods for adult and aging animals: Application of targeted patch clamp analysis and optogenetics. *Methods Mol. Biol.* **1183**, 221–242 (2014).
78. Y. Hao, S. Hao, E. Andersen-Nissen, W. M. Mauck 3rd, S. Zheng, A. Butler, M. J. Lee, A. J. Wilk, C. Darby, M. Zager, P. Hoffman, M. Stoeckius, E. Papalexi, E. P. Mimitou, J. Jain, A. Srivastava, T. Stuart, L. M. Fleming, B. Yeung, A. J. Rogers, J. M. McElrath, C. A. Blish, R. Gottardo, P. Smibert, R. Satija, Integrated analysis of multimodal single-cell data. *Cell* **184**, 3573–3587.e29 (2021).
79. H. Wickham, *ggplot2: Elegant Graphics for Data Analysis* (Springer, 2016).
80. Z. Gu, R. Eils, M. Schlesner, Complex heatmaps reveal patterns and correlations in multidimensional genomic data. *Bioinformatics* **32**, 2847–2849 (2016).
81. M. Munisamy, N. Mukherjee, L. Thomas, A. T. Pham, A. Shakeri, Y. Zhao, J. Kolesar, P. P. N. Rao, V. M. Rangnekar, M. Rao, Therapeutic opportunities in cancer therapy: Targeting the p53-MDM2/MDMX interactions. *Am. J. Cancer Res.* **11**, 5762–5781 (2021).

82. G. Tin, T. Mohamed, A. Shakeri, A. T. Pham, P. P. N. Rao, Interactions of selective serotonin reuptake inhibitors with β-amyloid. *ACS Chem. Neurosci.* **10**, 226–234 (2019).
83. L. Gold, D. Ayers, J. Bertino, C. Bock, A. Bock, E. N. Brody, J. Carter, A. B. Dalby, B. E. Eaton, T. Fitzwater, D. Flather, A. Forbes, T. Foreman, C. Fowler, B. Gawande, M. Goss, M. Gunn, S. Gupta, D. Halladay, J. Heil, J. Heilig, B. Hicke, G. Husar, N. Janjic, T. Jarvis, S. Jennings, E. Katilius, T. R. Keeney, N. Kim, T. H. Koch, S. Kraemer, L. Kroiss, N. Le, D. Levine, W. Lindsey, B. Lollo, W. Mayfield, M. Mehan, R. Mehler, S. K. Nelson, M. Nelson, D. Nieuwlandt, M. Nikrad, U. Ochsner, R. M. Ostroff, M. Otis, T. Parker, S. Pietrasiewicz, D. I. Resnicow, J. Rohloff, G. Sanders, S. Sattin, D. Schneider, B. Singer, M. Stanton, A. Sterkel, A. Stewart, S. Stratford, J. D. Vaught, M. Vrkljan, J. J. Walker, M. Watrobka, S. Waugh, A. Weiss, S. K. Wilcox, A. Wolfson, S. K. Wolk, C. Zhang, D. Zichi, Aptamer-based multiplexed proteomic technology for biomarker discovery. *PLOS ONE* **5**, e15004 (2010).
84. E. Assarsson, M. Lundberg, G. Holmquist, J. Bjorkesten, S. B. Thorsen, D. Ekman, A. Eriksson, E. Rennel Dickens, S. Ohlsson, G. Edfeldt, A. C. Andersson, P. Lindstedt, J. Stenvang, M. Gullberg, S. Fredriksson, Homogenous 96-plex PEA immunoassay exhibiting high sensitivity, specificity, and excellent scalability. *PLOS ONE* **9**, e95192 (2014).

Acknowledgments: We thank R. Britton, M. Kilinc, N. Huber, C. Tun, D. Le, H. Hackbart, I. Gallagher, and C. Yang for technical assistance; P. R. P. Nekkar for molecular modeling; S. Ahadi, N. Hin, and I. Kosti for statistical review; B. Von Melchert for vivarium support; and S. S. Minami, V. Kheifets, and T. Wyss-Coray for critical discussion on the experiments and careful reading and editing of the manuscript. We also thank A. Cano, M. Marquié, A. Ruiz, and M. Boada at Ace Alzheimer Center Barcelona for providing us with human AD plasma samples. **Funding:** This research did not receive any specific grant from funding agencies in the public, commercial, or not-for-profit sectors. **Author contributions:** Conceptualization: E.C., D.P.L., S.B., and M.K.C. Investigation: J.M.A., S.V.R., A.T.L., N.V.V., S.R., A.L.N., D.P.L., E.C., and M.K.C. Methodology: J.M.A., N.V.V., D.Y.K., R.H., B.S., D.P.L., and M.K.C. Data curation: N.V.V., D.Y.K., B.S., and D.P.L. Visualization: J.M.A., S.V.R., S.R., N.V.V., R.H., D.P.L., and M.K.C. Supervision: D.P.L., E.C., S.B., and M.K.C. Writing: J. M.A., D.P.L., and M.K.C. **Competing interests:** All authors were full-time employees of Alkahest Inc. at the time that they contributed to the experiments in this manuscript. M.K.C., E.C., and B.S. are inventors on U.S. patents 11,344,542 and 11,426,399 held by Alkahest that covers the treatment of aging-associated disease with modulators of LTA4H. M.K.C., E.C., and R.H. are inventors on U.S. patent application 17,700,804 submitted by Alkahest that covers the treatment or prevention of aging associated disease with benzodioxane modulators of LTA4H. **Data and materials availability:** All data needed to evaluate the conclusions in the paper are present in the paper and/or the Supplementary Materials. Next-generation sequencing data have been deposited in the database Dryad and available for download using the following links: Leone, Dino; Campbell, Meghan (2023). Leukotriene A4 hydrolase inhibition improves age related cognitive decline via modulation of synaptic function, part 1 [Dataset]. Dryad. https://doi.org/10.5061/dryad.fbg79cp1c. Leone, Dino; Campbell, Meghan (2023). Leukotriene A4 hydrolase inhibition improves age related cognitive decline via modulation of synaptic function, part 2 [Dataset]. Dryad. https://doi.org/10.5061/dryad.51c59zwdv.

Submitted 8 May 2023
Accepted 13 October 2023
Published 17 November 2023
10.1126/sciadv.adf8764